exoALMA. VI. Rotating under pressure: rotation curves, azimuthal velocity substructures, and gas pressure variations

Stadler, J.; Benisty, M.; Winter, A.J.; Izquierdo, A.F.; Longarini, C.; Galloway-Sprietsma, M.; ... ; Zawadzki, B.

The Astrophysical Journal Letters, 984:L11 (29pp), 2025 May 1 https://doi.org/10.3847/2041-8213/adb152

exoALMA. VI. Rotating under Pressure: Rotation Curves, Azimuthal Velocity Substructures, and Gas Pressure Variations

Jochen Stadler[1], Myriam Benisty[1,2], Andrew J. Winter[1,2], Andrés F. Izquierdo[3,4,5,26], Cristiano Longarini[6,7], Maria Galloway-Sprietsma[3], Pietro Curone[7,8], Sean M. Andrews[9], Jaehan Bae[3], Stefano Facchini[7], Giovanni Rosotti[7], Richard Teague[10], Marcelo Barraza-Alfaro[10], Gianni Cataldi[11], Nicolás Cuello[12], Ian Czekala[13], Daniele Fasano[1], Mario Flock[2], Misato Fukagawa[11], Himanshi Garg[14], Cassandra Hall[15,16,17], Iain Hammond[14], Thomas Hilder[14], Jane Huang[18], John D. Ilee[19], Kazuhiro Kanagawa[20], Geoffroy Lesur[12], Giuseppe Lodato[7], Ryan A. Loomis[21], Francois Menard[12], Ryuta Orihara[20], Christophe Pinte[12,14], Daniel J. Price[14], Hsi-Wei Yen[22], Gaylor Wafflard-Fernandez[12], David J. Wilner[9], Lisa Wölfer[10], Tomohiro C. Yoshida[11,23], and Brianna Zawadzki[24,25]
[1] Université Côte d'Azur, Observatoire de la Côte d'Azur, CNRS, Laboratoire Lagrange, France; jochen.stadler@oca.eu
[2] Max-Planck Institute for Astronomy (MPIA), Königstuhl 17, 69117 Heidelberg, Germany
[3] Department of Astronomy, University of Florida, Gainesville, FL 32611, USA
[4] Leiden Observatory, Leiden University, P.O. Box 9513, NL-2300 RA Leiden, The Netherlands
[5] European Southern Observatory, Karl-Schwarzschild-Str. 2, D-85748 Garching bei München, Germany
[6] Institute of Astronomy, University of Cambridge, Madingley Road, Cambridge, CB3 0HA, UK
[7] Dipartimento di Fisica, Università degli Studi di Milano, Via Celoria 16, 20133 Milano, Italy
[8] Departamento de Astronomía, Universidad de Chile, Camino El Observatorio 1515, Las Condes, Santiago, Chile
[9] Center for Astrophysics — Harvard & Smithsonian, Cambridge, MA 02138, USA
[10] Department of Earth, Atmospheric, and Planetary Sciences, Massachusetts Institute of Technology, Cambridge, MA 02139, USA
[11] National Astronomical Observatory of Japan, 2-21-1 Osawa, Mitaka, Tokyo 181-8588, Japan
[12] Univ. Grenoble Alpes, CNRS, IPAG, 38000 Grenoble, France
[13] School of Physics & Astronomy, University of St. Andrews, North Haugh, St. Andrews, KY16 9SS, UK
[14] School of Physics and Astronomy, Monash University, Clayton, VIC 3800, Australia
[15] Department of Physics and Astronomy, University of Georgia, Athens, GA 30602, USA
[16] Center for Simulational Physics, University of Georgia, Athens, GA 30602, USA
[17] Institute for Artificial Intelligence, University of Georgia, Athens, GA, 30602, USA
[18] Department of Astronomy, Columbia University, 538 W. 120th Street, Pupin Hall, New York, NY 10027, USA
[19] School of Physics and Astronomy, University of Leeds, Leeds, LS2 9JT, UK
[20] College of Science, Ibaraki University, 2-1-1 Bunkyo, Mito, Ibaraki 310-8512, Japan
[21] National Radio Astronomy Observatory, 520 Edgemont Rd., Charlottesville, VA 22903, USA
[22] Academia Sinica Institute of Astronomy & Astrophysics, 11F of Astronomy-Mathematics Building, AS/NTU, No.1, Sec. 4, Roosevelt Rd, Taipei 10617, Taiwan
[23] Department of Astronomical Science, The Graduate University for Advanced Studies, SOKENDAI, 2-21-1 Osawa, Mitaka, Tokyo 181-8588, Japan
[24] Department of Astronomy, Van Vleck Observatory, Wesleyan University, 96 Foss Hill Drive, Middletown, CT 06459, USA
[25] Department of Astronomy & Astrophysics, Pennsylvania State University, 525 Davey Laboratory, University Park, PA 16802, USA
Received 2024 November 21; revised 2025 January 29; accepted 2025 February 1; published 2025 April 28

Abstract

The bulk motion of the gas in protoplanetary disks around newborn stars is nearly Keplerian. By leveraging the high angular and spectral resolution of the Atacama Large Millimeter/submillimeter Array (ALMA), we can detect small-scale velocity perturbations in molecular line observations caused by local gas pressure variations in the disk, possibly induced by embedded protoplanets. This Letter presents the azimuthally averaged rotational velocity and its deviations from Keplerian rotation (δv_ϕ) for the exoALMA sample, as measured in the ^{12}CO $J = 3$–2 and ^{13}CO $J = 3$–2 emission lines. The rotation signatures show evidence for vertically stratified disks, in which ^{13}CO rotates faster than ^{12}CO due to a distinct thermal gas pressure gradient at their emitting heights. We find δv_ϕ substructures in the sample on both small ($\sim$10 au) and large ($\sim$100 au) radial scales, reaching deviations up to 15% from background Keplerian velocity in the most extreme cases. More than 75% of the rings and 80% of the gaps in the dust continuum emission resolved in δv_ϕ are colocated with gas pressure maxima and minima, respectively. Additionally, gas pressure substructures are observed far beyond the dust continuum emission. For the first time, we determined the gas pressure derivative at the midplane from observations, and found it to align well with the dust substructures within the given uncertainties. Based on our findings, we conclude that gas pressure variations are likely the dominant mechanism for ring and gap formation in the dust continuum.

Unified Astronomy Thesaurus concepts: Protoplanetary disks (1300); Planet formation (1241); Planetary system formation (1257); Planetary-disk interactions (2204)

1. Introduction

The exceptional capabilities of the Atacama Large Millimeter/submillimeter Array (ALMA) have made it possible to measure the rotation of gas in protoplanetary disks and search for the kinematic footprints of embedded protoplanets (see review by C. Pinte et al. 2023). The rotational velocity of the gas v_ϕ orbiting a star of mass $M_\star$ at a given cylindrical radius R

[26] NASA Hubble Fellowship Program Sagan Fellow.

and height z assuming centrifugal balance is given by

$$\frac{v_\phi(R,z)^2}{R} = \frac{GM_\star R}{(R^2+z^2)^{3/2}} + \frac{1}{\rho_{\rm gas}}\frac{\partial P_{\rm gas}}{\partial R} + \frac{\partial \phi_{\rm gas}}{\partial R}, \quad (1)$$

where $\rho_{\rm gas}(R, z)$ is the gas density, $P_{\rm gas}(R, z)$ is the gas pressure, and $\phi_{\rm gas}(R, z)$ is the gravitational potential of the disk (e.g., T. Takeuchi & D. N. C. Lin 2002). The first term on the right-hand side of the equation describes the dominant contribution from the star.

Observationally, one measures the rotation curve from molecular line emissions which occurs from a given altitude in the disk. Thus, the dependence of the rotation curve on z can be inferred by measuring the emission layer height, as has been demonstrated for several systems (C. Pinte et al. 2018; C. J. Law et al. 2021; C. J. Law et al. 2023; T. Paneque-Carreño et al. 2023). The third term becomes important if the disk is sufficiently massive ($M_{\rm disk} \geqslant 0.1M_\star$; e.g., G. Lodato 2007; K. Kratter & G. Lodato 2016), in which case it will speed up the gas, in particular in the outermost regions of the disk enclosing the most of the disk's mass. In recent years, studies have leveraged this effect to determine the total disk mass (B. Veronesi et al. 2021; B. Veronesi et al. 2024; G. Lodato et al. 2023; S. M. Andrews et al. 2024; P. Martire et al. 2024).

The second term is the acceleration due to the gas pressure gradient. This is of particular importance as it is most sensitive to localized variations in the physical conditions of the gas. On a global scale, the pressure gradient decreases with radius, as do the gas density and temperature, which introduces sub-Keplerian rotation in the outermost disk radii. However, local vertical and radial modulations in temperature and density can result in both large- and small-scale perturbations to the velocity curve, and thus deviations from Keplerian rotation (e.g., K. A. Rosenfeld et al. 2013; C. Rab et al. 2020; S. M. Andrews et al. 2024; V. Pezzotta et al. 2025). Leveraging high spatial and spectral resolution ALMA observations, it is possible to measure these localized small-scale perturbations in the rotational velocity (R. Teague et al. 2018a, 2018b; G. P. Rosotti et al. 2020). Furthermore, the derivative of the midplane gas pressure determines the drift rate of dust particles (F. L. Whipple 1972; S. J. Weidenschilling 1977; T. Takeuchi & D. N. C. Lin 2002; L. Barrière-Fouchet et al. 2005; T. Birnstiel et al. 2010). As the dynamics of dust particles depends on the relative coupling to the gas, gas pressure minima and maxima can create gaps and rings in the millimeter continuum emission, respectively (e.g., S. J. Paardekooper & G. Mellema 2004; B. A. Ayliffe et al. 2012; P. Pinilla et al. 2012; G. Dipierro et al. 2015; J. Stadler et al. 2022). The observed continuum substructures can therefore be linked to local deviations from Keplerian rotation (R. Teague et al. 2018a; G. P. Rosotti et al. 2020).

Recently, A. F. Izquierdo et al. (2023) studied the kinematics of the MAPS sample (K. I. Öberg et al. 2021) and found that nine out of 11 continuum rings in the disks are colocated with gas pressure maxima, traced by deviations in v_ϕ. Earlier, A. F. Izquierdo et al. (2022) illustrated the correlation between gas pressure minima and line-width minima when observed through optically thick molecular lines. This correlation allows for robust detections of gaps in the gas surface density when examined in conjunction with the azimuthal velocity structure. These studies demonstrate that analyzing the rotation curves of disks can greatly enhance our understanding of the dynamics and evolution of planet-forming disks. Utilizing the exceptional data quality from the exoALMA Large Program (0.″1, 26 m s^{-1}; R. Teague et al. 2025), such analysis is especially valuable, as it provides insights into the (sub)structures, kinematics, and physical conditions of our sample of disks.[27]

This Letter presents the rotation curves for the 15 disks of the exoALMA sample, measured from ^{12}CO J = 3–2 and ^{13}CO J = 3–2 molecular line emission. Even though CS J = 7–6 has also been observed as part of the program, we focus our analysis on the CO lines since it is difficult to extract reliable v_ϕ for the CS line for most of the disks. We assess the evidence of vertical stratification and the deviations from Keplerian rotation in the sample. In particular, we aim to investigate whether substructures in the gas pressure cause the observed dust continuum substructures. The Letter is structured as follows. Section 2 illustrates the choice of molecular line data cubes studied, and Section 3 explains the methods applied to the data. In Sections 4 and 5, we present the results for the global disk properties and variations of the rotational velocity colocated with the dust substructures, respectively. Finally, we discuss our results in Section 6, and draw our conclusions in Section 7.

2. Data

The calibration and imaging of the ^{12}CO J = 3–2, ^{13}CO J = 3–2, and CS J = 7–6 molecular line data cubes used for the analysis in this work are presented in detail in R. A. Loomis et al. (2025). For each molecule and disk there are three sets of continuum-subtracted image cubes. Namely, these are the fiducial images (beam size = 0.″15), high-resolution images (beam size < 0.″15), and high-surface-brightness sensitivity images (beam size = 0.″30; see R. Teague et al. 2025 for details). This Letter utilizes all three image sets tailored to the specific disk region and scientific objectives we intend to explore, which motivates the necessary angular resolution and sensitivity. Specifically, we must find a balance between achieving high sensitivity for the faint outer disks and high angular resolution for the structure of the inner disk. To address this issue, in Section 4 we employ the high-surface-brightness sensitivity images to study the global disk properties on large scales, while in Section 5 we use the high-resolution images to investigate small-scale deviations from Keplerian rotation in the innermost disk regions colocated with the dust continuum. To this end, we spatially divide our analysis into two disk regions (inner versus outer), separated at $0.9R_{\rm d,90}$, where $R_{\rm d,90}$ is the radius enclosing 90 % of the continuum flux (see P. Curone et al. 2025). This separation essentially divides the disks into an inner region colocated with the continuum emission and an outer one without large (millimeter) dust grains and substructures.

In order to accurately resolve the small-scale variations of the rotational velocities in the inner regions of the disks colocated with the continuum substructures, we require an angular resolution of at least half the major axis of the gas beam ($\rm beam_{major}$) to encompass the radial width of a gap or ring in the continuum. This is achieved with 0.″10 < $\rm beam_{major}$ ⩽ 0.″15, channel spacings of 100–200 m s^{-1}, and a signal-to-noise ratio (SNR) of ⩾5 in the CO moment maps. On the other hand, to robustly measure the rotational velocity across the entire radial extent of the disk, we choose larger beam sizes (0.″15–0.″30) and channel spacings (100–200 m s^{-1}) to achieve a high SNR to

[27] https://www.exoalma.com

resolve the whole spatial extent of the disk. In Figure E1, we show that these different choices of angular resolution do not negatively affect the analysis products over the scales of interest (see also R. Teague et al. 2025). A table with the employed data cubes for each disk and analysis can be found in R. A. Loomis et al. (2025), and the dust continuum substructures and their properties are reported in P. Curone et al. (2025).

3. Methods

3.1. Line Centroid Velocity Extraction

To accurately determine the line-of-sight velocity $\upsilon_{\rm los}$, a precise measurement of the centroid of the peak of the line profile at every pixel is required. We modeled each disk and molecular line using the code `discminer` (A. F. Izquierdo et al. 2021), which fits a Keplerian model to the local line profile for each channel of a molecular line data cube. The strength of `discminer` lies in its ability to model both the upper (front) and lower (back) surface emission. This is important for mid- to high-inclined sources ($i \sim 30°-60°$), where the line profile is generally double-peaked due to the contribution of both surfaces. With a model for both emission surfaces at hand, it is possible to disentangle them to get a more accurate fit to the centroid of the line peak of the front surface. This is of particular importance in regions of the disk where the emission of the back surface of the disk becomes brighter than the upper surface or overlaps with it. In those cases with a line profile showing two components, we fit a two-component bell function to the line profile, which is essentially a Gaussian with one additional parameter that adds flexibility in controlling the line slope. For disks that only show a single-peaked line profile, we generally fit a single Gaussian to determine the line centroid. The procedure of this newly improved double-bell kernel is presented in detail in A. F. Izquierdo et al. (2025), as well as an overview of the choice of applied moment maps for each disk and molecular line.

3.2. Rotational Velocity

The line-of-sight velocity can be decomposed into its disk-frame cylindrical components υ_ϕ, υ_r, and υ_z. The respective projection of these components along the line of sight is given by

$$\upsilon_{\rm los} = \upsilon_{\phi,{\rm proj}} + \upsilon_{r,{\rm proj}} + \upsilon_{z,{\rm proj}} + \upsilon_{\rm LSR}, \tag{2}$$

$$\upsilon_{\phi,{\rm proj}} = \upsilon_\phi \cos(\phi)\sin(i) \cdot sgn_{\rm rot}, \tag{3}$$

$$\upsilon_{r,{\rm proj}} = -\upsilon_r \sin(\phi)\sin(i), \tag{4}$$

$$\upsilon_{z,{\rm proj}} = -\upsilon_z \cos(i), \tag{5}$$

where $\upsilon_{\rm LSR}$ is the systemic velocity, ϕ the polar angle of the disk measured counterclockwise from the redshifted major axis, $i \in [-90°, 90°]$ the disk inclination, and $sgn_{\rm rot}$ denotes whether the disk rotates clockwise (+1) or counterclockwise (−1) (see A. F. Izquierdo et al. 2025 for the adopted geometric conventions).

We follow the analytical approach in A. F. Izquierdo et al. (2023) to extract the individual components from the $\upsilon_{\rm los}$. First, we extract the geometric parameters, including the offset from the center of the disk, the inclination, the position angle, and the systemic velocity of each disk, from the best-fit parameters obtained from the ^{12}CO `discminer` fits (A. F. Izquierdo et al. 2025). Having these parameters, we can project a 2D grid onto our line centroid velocity moment maps. Next, we infer the rotational velocity v_ϕ for a specified radial annulus by taking the azimuthal average of the absolute value of the centroid velocity map υ_0 after subtracting $\upsilon_{\rm LSR}$. This assumes the rotational velocity to be azimuthally symmetric around the disk's minor axis and dominant over the radial and vertical ones:

$$\upsilon_\phi = \frac{\psi}{4\sin\frac{\psi}{4}\sin|i|}\langle|\upsilon_0 - \upsilon_{\rm LSR}|\rangle_\psi, \tag{6}$$

where ψ denotes the angular extent of the azimuthal section where the averages are computed (see Appendix C in A. F. Izquierdo et al. 2023 for derivation). We mask 30° around both sides of the disk's minor axis, due to uncertainties in the deprojection at locations where $\cos(\phi)$ tends to zero. We extract radial profiles of υ_ϕ starting from one major beam size from the disk center in steps of a quarter the major beam size and report the uncertainties of the profiles as the standard deviation normalized by the square root of independent beams along each radial annulus (A. F. Izquierdo et al. 2023). Finally, we apply a Savitzky–Golay filter of first order with a window length of one major beam size for smoothing and visual clarity of the plots in the main text. The quantitative analysis, however, is conducted on the raw data.

The deviations from Keplerian circular motion $\delta\upsilon_\phi$ can then be obtained by subtracting the Keplerian rotation $\delta\upsilon_\phi = \upsilon_\phi - \upsilon_{\rm k}$, given by

$$\upsilon_{\rm k}(R, z) = \sqrt{\frac{GM_\star R^2}{(R^2 + z^2)^{3/2}}}. \tag{7}$$

Unless explicitly stated otherwise, we obtain the stellar mass from the best-fit parameter of the `discminer` fits for each molecular line, which is available for all sources (A. F. Izquierdo et al. 2025). However, it is important to note that these $M_\star$ values should not be viewed as a *true* stellar mass since `discminer` only prescribes a pure Keplerian disk model (see Equation (7)) and does not specifically account for the pressure and self-gravity terms of Equation (1). This leads to differences on the order of ∼5% between these best-fit values and the true stellar masses, as shown for a subset of our sample in C. Longarini et al. (2025). In the following, we define $M_\star$ in Equation (7) as the *kinematic* stellar mass and elaborate on this further in the discussion.

The emission heights of CO molecules (that go into Equation (7)) usually arise from $z/R \approx 0.2$–0.3 in disks (C. J. Law et al. 2023; M. Galloway-Sprietsma et al. 2025). The elevation z of the upper and lower emission surface, above and below the disk midplane, was modeled as an exponentially tapered power law:

$$z(R) = z_0\left(\frac{R}{100\ {\rm au}}\right)^{p_z}\exp\left[-\left(\frac{R}{R_t}\right)^{q_t}\right], \tag{8}$$

where z_0, p_z, R_t, and q_t are fitting parameters. For the analysis in this Letter, we use the best-fit parameters of the `discminer` surface fits, compatible with our velocity analysis framework.

The extraction of the other two velocity components, υ_r and υ_z, will be presented in a forthcoming paper.

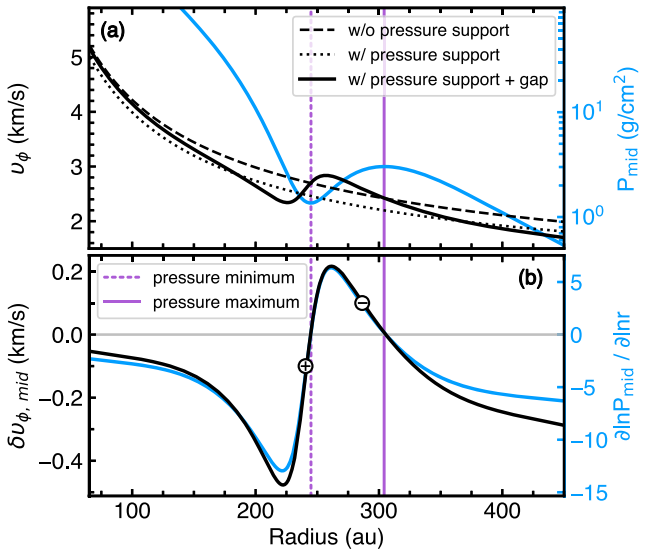

Figure 1. (a) Azimuthal velocities (left axis, black lines) and midplane pressure (right axis, blue lines), (b) along with the deviations from Keplerian rotation and the first radial derivative of the pressure, for a hydrodynamic model with an imposed Gaussian gap in the pressure at $R = 240$ au. The pressure minimum and maximum locations are marked with vertical purple dashed and full lines, respectively. The circles in (b) mark the sign of the radial derivative of $\delta\upsilon_\phi$ coinciding with the pressure minimum ($\oplus$) and maximum ($\ominus$), respectively.

3.3. Pressure Variations

Both the stellar and self-gravity terms in Equation (1) solely introduce a large-scale component to the rotational velocity, hence, if observed, small-scale substructures in υ_ϕ can be attributed to pressure variations.

The radial gradient of the pressure profile can be directly related to the observed deviation in Keplerian rotation $\delta\upsilon_\phi$. For now, we neglect the disk self-gravity, which is subdominant to the pressure (S. M. Andrews et al. 2025; C. Longarini et al. 2025). However, it is important to note that we will consider it later when calculating the pressure gradient at the midplane in Section 6.1. Neglecting $\phi_{\rm gas}$ allows us to rearrange Equation (1) as

$$\left.\frac{\partial \ln P(R,\,z)}{\partial \ln R}\right|_{z=z_{\rm emit}} = \frac{\upsilon_\phi^2 - \upsilon_{\rm k}^2}{c_{\rm s}^2} \approx 2\frac{\upsilon_{\rm k}^2}{c_{\rm s}^2}\frac{\delta\upsilon_\phi}{\upsilon_{\rm k}}, \tag{9}$$

where we have approximated $\upsilon_\phi \simeq \upsilon_{\rm k}$ to first order, and introduced the sound speed, $c_{\rm s}$, as $P = \rho_{\rm gas} c_{\rm s}^2$. The sound speed is related to temperature by

$$c_{\rm s}^2(R,\,z) = \frac{k_{\rm B} T(R,\,z)}{\mu m_{\rm p}}, \tag{10}$$

where $k_{\rm B}$ the Boltzmann constant and $\mu = 2.3$ the mean molecular weight for the proton mass $m_{\rm p}$.

To demonstrate how pressure gradient and azimuthal velocity (or its gradient) are related to each other, we set up a toy model. Specifically, we set the background disk density and temperature structures identical to the ones used for the HD 163296 disk as presented in R. Teague et al. (2019), and impose a Gaussian gap centered at $R = 240$ au, with a radial width of 50 au and the maximum depth at the gap center of 90%. Following R. Teague et al. (2019), the rotational velocity is numerically computed such that the disk is in centrifugal balance. Figure 1 illustrates the expected variation of the rotational velocity for the disk having a Gaussian gap. We highlight that this toy model is for illustration purposes, demonstrating stronger pressure perturbations than those typically observed in our data set.

In panel (a), we plot the background rotation for a disk with (dotted black line) and without (dashed black line) pressure support, which corresponds to the first and second terms, or only the first term of Equation (1), respectively. From the model, we expect $\delta\upsilon_{\phi,\rm mid}$ and $\partial \ln {\rm P}_{\rm mid}/\partial \ln {\rm R}$ at the midplane (subscript "mid") to be equal to zero at the locations of the pressure minima and maxima, as shown in Figure 1(b). This holds assuming that we know exactly the stellar mass. However, as pointed out in Section 3.2, disentangling the various contributions to the rotational velocity (Equation (1)) makes it difficult to constrain $M_\star$ precisely. This in turn results in a vertical shift in $\delta\upsilon_{\phi,\rm mid}$, thus we cannot accurately identify the pressure minima or maxima at locations of $\delta\upsilon_{\phi,\rm mid} = 0$. Similar to G. P. Rosotti et al. (2020), we circumvent this problem by investigating the sign of the radial derivative of $\delta\upsilon_\phi$. Hence, around the location of a pressure minimum, we expect $\delta\upsilon_\phi$ to increase radially ($\oplus$), and the opposite for a pressure maximum ($\ominus$; compare to markers in Figure 1(b)). This diagnostic will be used to infer the pressure minima and maxima presented in this work. In Section 6.1, we will also infer the midplane pressure derivative for a subset of our sample.

3.4. Properties of $\delta\upsilon_\phi$ Substructures

In Section 5, we present $\delta\upsilon_\phi$ variations across the full disk extent, where numerous substructures due to pressure variations are present. However, we focus on the question of whether pressure substructures align with the continuum gaps and rings. Thus, we report quantitative properties of $\delta\upsilon_\phi$ substructures only when (1) they are colocated with continuum substructures. We further restrict our analysis to (2) axisymmetric continuum substructures (discarding crescents) at locations that are well resolved. The latter means we only consider "strong" dust substructures that satisfy (3) a contrast $I_{\rm D}/I_{\rm B} < 0.8$ between their gap ($I_{\rm D}$) and ($I_{\rm B}$) ring intensity, discarding very subtle gap–ring pairs ($I_{\rm D}/I_{\rm B} < 0.96$ in P. Curone et al. 2025). Additionally, the continuum substructure must exhibit (4) a radially increasing (at dust gaps) or decreasing (at dust rings) $\delta\upsilon_\phi$ profile for two consecutive data points. Finally, (5) the radial extent of the $\delta\upsilon_\phi$ perturbation must exceed half of a major beam size. For $\delta\upsilon_\phi$ substructures satisfying all of the above five criteria, we measure their width as the radial extent between two data points $(\delta\upsilon_{\phi,\rm min}(r_{\rm min}),\ \delta\upsilon_{\phi,\rm max}(r_{\rm max}))$ along which $\partial\delta\upsilon_\phi/\partial R$ stays either positive or negative. The center between these two points then gives the radial location of the substructure; their amplitude is reported as $A = |\delta\upsilon_{\phi,\rm max} - \delta\upsilon_{\phi,\rm min}|$, and its uncertainty as $\Delta A = (\Delta\delta\upsilon_{\phi,\rm max}^2 + \Delta\delta\upsilon_{\phi,\rm min}^2)^{1/2}$. We assume the uncertainties in the measurements of the radial location and width to be half the FWHM of the major beam size.

We comment on continuum substructures that do not satisfy one or more of the above criteria in Table 1 of Appendix A. Our measurement of the $\delta\upsilon_\phi$ gap's amplitude, width, and radial location follows the approach presented in H.-G. Yun et al. (2019). We can thus use their derived relations to convert the gap $\delta\upsilon_\phi$ amplitudes into estimates of a planet mass potentially driving the perturbation, as presented in Appendix B.

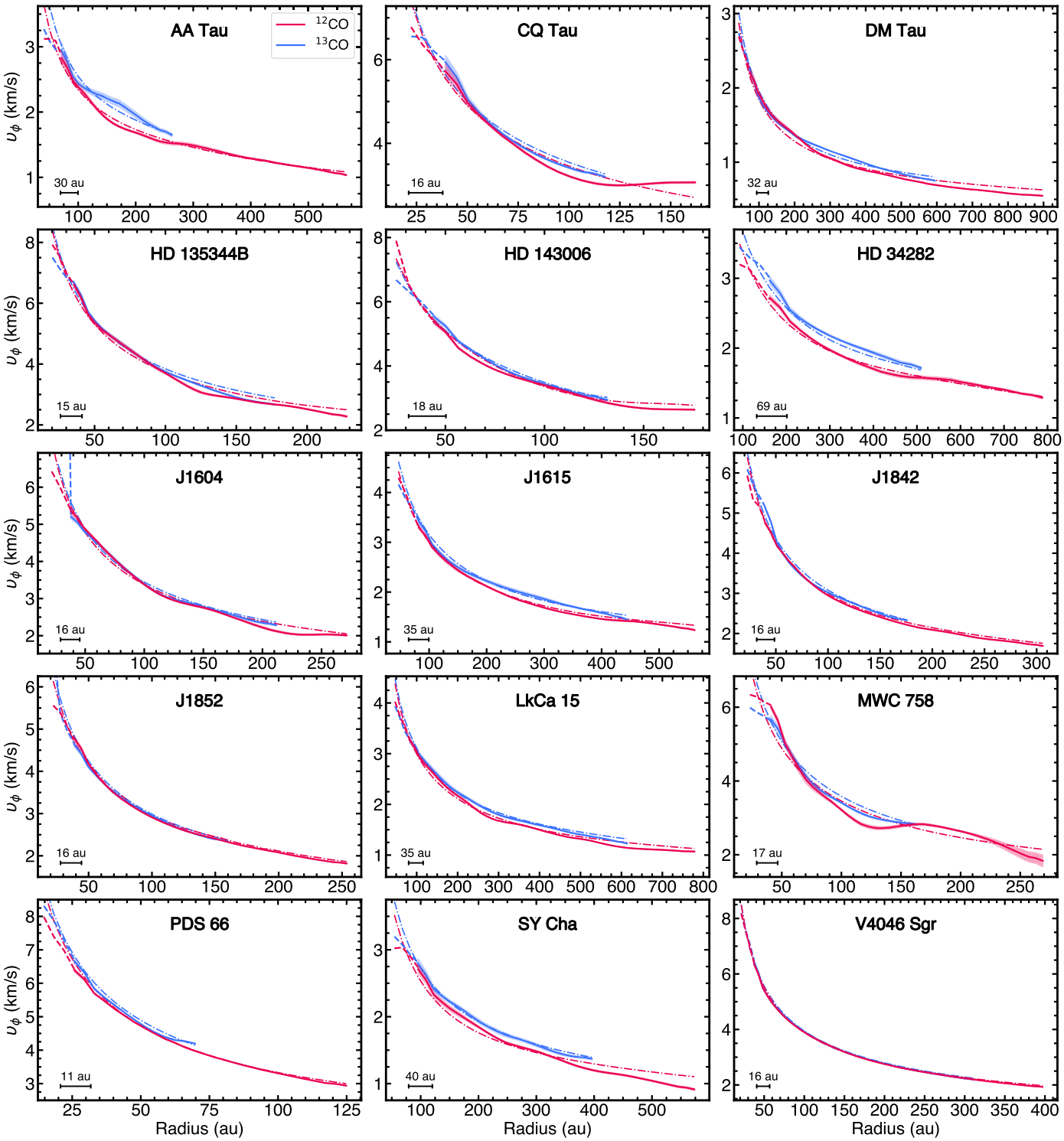

Figure 2. Rotation curves $\upsilon_\phi(R, z(R))$ measured from ^{12}CO (red) and ^{13}CO (blue), shown for all sources using the high-surface-brightness sensitivity images. For radii smaller than twice the beam size, the curves are plotted with dashed lines due to uncertainties in the velocity extraction. The colored shaded area of the lines shows the standard deviation within each extracted radial annulus usually on the order of ≈10–50 m s^{-1}. The fitted Keplerian rotation is plotted as a thin dashed–dotted line for each molecule, respectively (Equation (7)). The beam size for both molecular lines is plotted in the lower-left corner.

4. Global Disk Properties

4.1. Vertical Thermal Stratification

In Figure 2, we show the rotation curves for the molecular lines ^{12}CO $J = 3$–2 and ^{13}CO $J = 3$–2 for all 15 disks of the sample using the high-surface-brightness sensitivity images. We focus our analysis on these lines and omit the rotation curves of the CS $J = 7$–6 line, which has also been observed as part of the program since it is difficult to extract reliable υ_ϕ for most of the disks due to a combination of limited angular resolution and the SNR of the line. Nonetheless, the retrieved CS rotation curves can be found in Figure E2 of Appendix E. As seen in Figure 2, we can infer ^{12}CO and ^{13}CO υ_ϕ out to radial extents of several hundreds of au. For the largest disks in

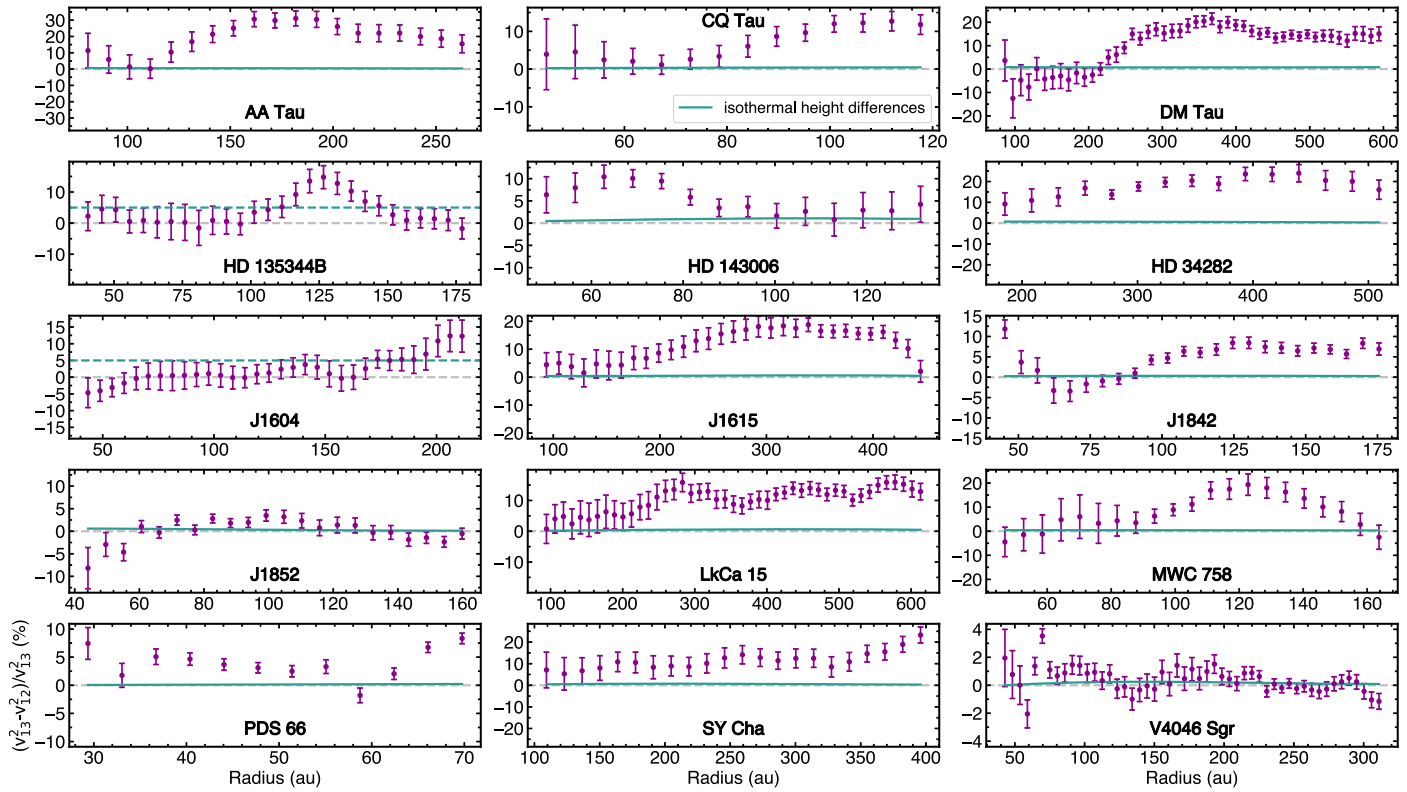

Figure 3. Level of vertical stratification between the ^{12}CO and ^{13}CO rotation curves (see Equation (11)) outside of two beam sizes from the center. The turquoise line displays the expected isothermal velocity shift solely due to the differences in emitting height (Equation (11)).

the sample, LkCa 15 and DM Tau, we trace the ^{12}CO rotation out to about 800 and 900 au, respectively.

It is evident that the ^{12}CO and ^{13}CO rotation curves do not match. This discrepancy may arise from the fact that they trace distinct heights and stellar potentials in the disks, or from differences in their thermal pressure gradient at those heights (essentially stellar versus pressure term in Equation (1)). The earlier can be quantified following the approach of P. Martire et al. (2024), who studied the effect of vertical *thermal* stratification on rotation curves. First, we plot the relative differences of the squared rotational velocity for ^{12}CO ($\upsilon_{\phi,12}$) and ^{13}CO ($\upsilon_{\phi,13}$) in Figure 3. Now, we hypothetically assume that the disks are vertically isothermal, thus the differences between both rotation curves should be solely due to their differences in emission height. This can be expressed as follows:

$$\frac{\upsilon_{\phi,13}^2 - \upsilon_{\phi,12}^2}{\upsilon_{\rm k}^2} = -q_{\rm mid}\frac{\sqrt{1+z_{12}^2/R^2} - \sqrt{1+z_{13}^2/R^2}}{\sqrt{(1+z_{13}^2/R^2)(1+z_{12}^2/R^2)}}, \quad (11)$$

(P. Martire et al. 2024, their Equation (23)), where $q_{\rm mid}$ is the radial temperature power-law index at the midplane obtained from M. Galloway-Sprietsma et al. (2025), and z_{12} and z_{13} denote the `discminer` emission height for ^{12}CO and ^{13}CO, respectively. For the sources where no 2D temperature structure and thus no $q_{\rm mid}$ could be derived, we set $q_{\rm mid} = -0.32$, which is the mean of our sample. Lastly, for HD 135344B and J1604, no emission surface could be extracted due to their face-on nature. For those cases, we estimate an upper limit of the velocity shift for the right-hand side of Equation (11) following P. Martire et al. (2024), which assumes that for both CO molecules $z/R < 0.5$ holds. Then the upper limit for the right-hand side becomes <5%. This expected isothermal velocity shift due to differences in emitting height is plotted as a turquoise line in Figure 3.

In Figure 3, it is evident that for the majority of the sample the gas at the emission surface traced by ^{13}CO rotates faster than ^{12}CO, and the differences are larger than can be explained by differences in gravity assuming a constant temperature. Therefore, we can infer that the thermal pressure gradient differs at distinct heights in the disks. In simpler terms, vertical thermal stratification is noticeable in most of the disks. It is particularly pronounced for AA Tau, DM Tau, HD 34282, J1615, LkCa 15, and SY Cha, the largest disks in the sample. The exceptions are J1852, V4046 Sgr, and the face-on sources (HD 135344B, HD 143006, and J1604), where the ratio is around or below the isothermal height differences line. These results suggest a dependency with orbital radius for this method, which we discuss later in Section 6.4.

4.2. Pressure Drop-off in the Outer Disk

Assuming the disks are in centrifugal balance, we expect $\delta\upsilon_\phi$ variations to be mostly driven by modulations in the underlying pressure structure. In this section, we focus on the ^{12}CO molecular line to investigate the large-scale pressure modulations, as it offers higher sensitivity in the outermost regions of the disk. In Figure 4, we present the ^{12}CO radial $\delta\upsilon_\phi$ profiles showing the deviation from Keplerian rotation in the outer disk beyond the continuum, using the high-surface-brightness sensitivity images. The ^{13}CO $\delta\upsilon_\phi$ profiles are presented in Figure E3 of Appendix E, which show similar features to the ^{12}CO profiles though not tracing as far out in radius. At first

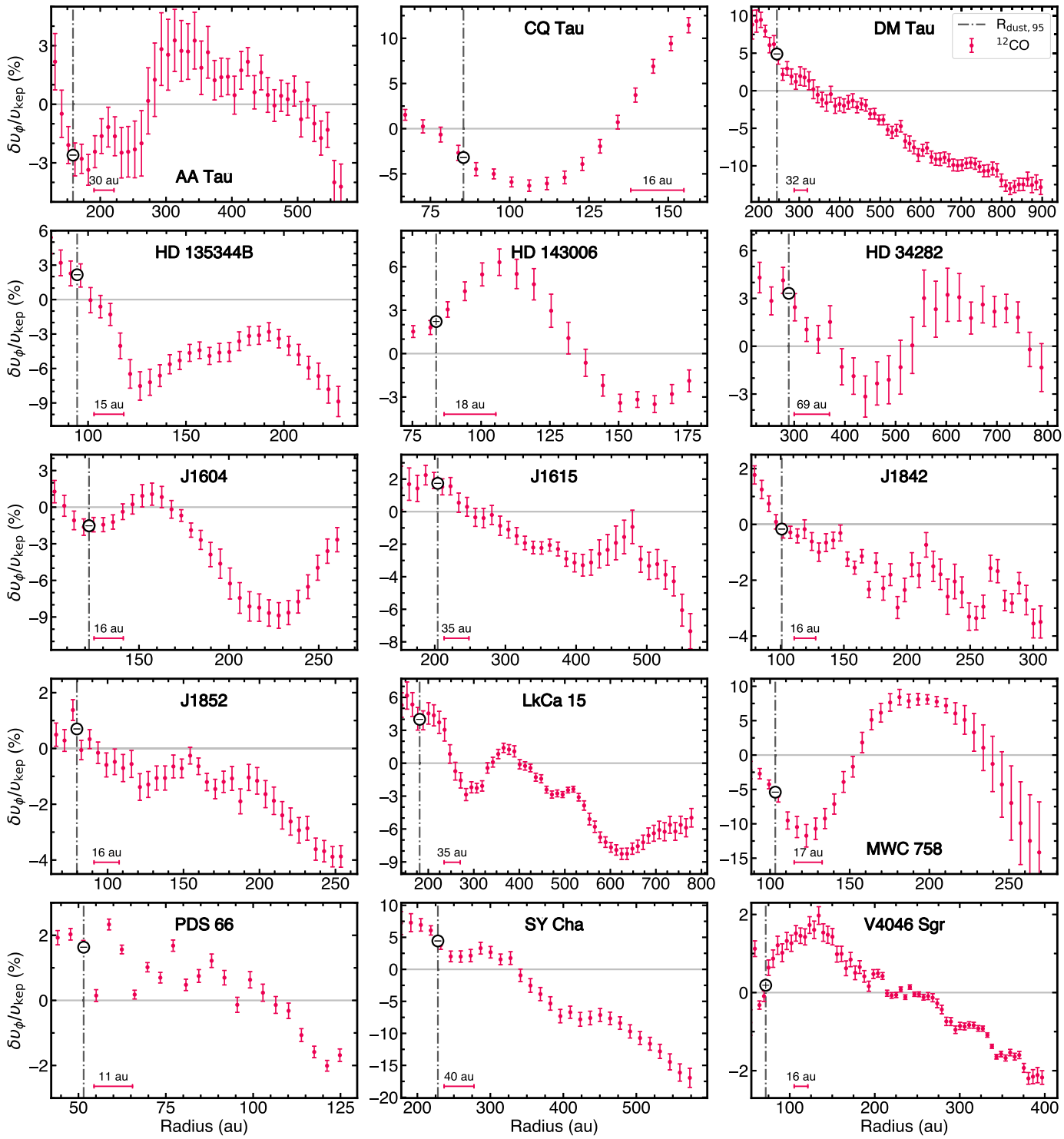

Figure 4. Radial profiles of δv_ϕ for ^{12}CO $J = 3$–2 of all sources focused on the region beyond the continuum substructures using the high-surface-brightness sensitivity images. The error bars show the standard deviation within each extracted radial annulus. The vertical dashed–dotted line indicates the radius that encompasses 95% of the continuum emission, with the signs of the radial derivatives of δv_ϕ marked at this location. The beam size is shown in the lower-left corner. The ^{13}CO δv_ϕ radial profiles can be found in Figure E3 of Appendix E.

glance, one can see numerous substructures in the δv_ϕ profiles for nearly all of the disks.

Most of the disks show an overall declining δv_ϕ slope and sub-Keplerian rotation in the outer-disk regions. This is as expected due to the pressure falloff, since the temperature and the density of the disk decrease with radius. For a power-law density profile, this would introduce only a minor deviation of about 1%–2% v_k (K. A. Rosenfeld et al. 2013; S. M. Andrews et al. 2024). However, if the density drops off exponentially (e.g., D. Lynden-Bell & J. E. Pringle 1974), the disk would experience a more substantial slowdown of the gas rotation, which has been discussed in detail by C. P. Dullemond et al. (2020, see their Section 4). They showed that a sharp exponential cutoff in the disk density distribution ($\gamma > 1$ for

a Lynden-Bell & Pringle Σ profile), reminiscent of the disk's outer edge, leads to a strong negative pressure gradient and thus significant sub-Keplerian rotation. The most striking examples of this effect are DM Tau and SY Cha, where the ^{12}CO Keplerian rotation slows down by more than 10% and 15% at their outermost radii, respectively, tracing their outer-disk edges. Nevertheless, half of the sample only shows deviations on the order of a few percent Keplerian on large radial scales in their ^{12}CO $\delta\upsilon_\phi$ profiles.

Our findings of sub-Keplerian rotation in the outer regions of the disk are consistent with the self-consistent modeling of the CO rotation curves presented in C. Longarini et al. (2025). In their study, they fitted the exponential tapering radius, which indicates where the gas density and pressure fall off, and typically found this radius to be several hundred au closer in than the edge of the disk. The exceptions to the previously described behavior of $\delta\upsilon_\phi$ are CQ Tau and MWC 758, who exhibit super-Keplerian rotation in their outer-disk regions due to strong asymmetric and non-Keplerian motions, visible as prominent spiral morphology in their velocity residuals (A. F. Izquierdo et al. 2025).

5. Rotational Velocity Variations at Dust Substructures

5.1. $\delta\upsilon_\phi$ Curves

In Figure 5, we present the deviations from Keplerian rotation for the ^{12}CO molecular line in the innermost disk regions coinciding with the dust continuum substructures (P. Curone et al. 2025). The ^{13}CO $\delta\upsilon_\phi$ profiles are shown in Figure E4 of Appendix E. For both molecular lines, we use the high-resolution images ($\mathrm{beam_{major}} \leqslant 0\farcs15$, presented in R. Teague et al. 2025) to access these radii and to radially resolve υ_ϕ at the underlying dust substructures. Similar to Figure 4, we also observe many $\delta\upsilon_\phi$ substructures in the inner-disk regions, which we report in Table 2 as outlined in Section 3.4. We decided only to show the profiles starting at a radius of two major beam sizes from the disk center since we resolve the circumference of closer-in annuli only by less than 12 major beam sizes. This limited angular resolution leads to artificial sub-Keplerian motion and large uncertainties within each of those inner radial bins due to beam-smearing and velocity-mixing effects (e.g., S. M. Andrews et al. 2024; T. Hilder et al. 2025), which are discussed in more detail in Section 6.3. The outer plotting limit is set to $0.9R_{\mathrm{dust,90}}$, which is the radius enclosing 90% of the continuum emission.

It is apparent that most of the transition disks (HD 34282, LkCa 15, MWC 758, and SY Cha) show radially increasing $\delta\upsilon_\phi$ profiles in their dust cavities, expected from density gaps at these locations. The exceptions of super-Keplerian velocities paired with radially decreasing $\delta\upsilon_\phi$ profiles for ^{12}CO in the transition disks of J1604 and HD 143006 can be attributed to highly non-Keplerian motions induced by warps and/or radial flows observed in these cavities (K. A. Rosenfeld et al. 2014; J. Stadler et al. 2023). For some disks, our angular resolution (number of independent beams along an annulus) and SNR are insufficient to assess their innermost cavities or dust substructures (e.g., CQ Tau or V4046).

5.2. Pressure Variations

In this section, we investigate the pressure substructures of the disks by analyzing the radial derivative of $\delta\upsilon_\phi$ as discussed in Section 3.3. Our goal is to determine whether the observed continuum gaps and rings align with the pressure minima and maxima, respectively (refer to Figure 1(c)). In Figure 6, we present the ^{12}CO $\delta\upsilon_\phi$ profiles for four selected targets, where the sign of $\partial\delta\upsilon_\phi/\partial R$ at the continuum substructures matches the theoretical expectations: $\partial\delta\upsilon_\phi/\partial R$ has a negative sign at the location of the continuum ring and a positive sign at a gap, as highlighted via the signs on the solid curves in Figure 6. For dust substructures exhibiting this theoretical behavior, indicating a decrease in $\delta\upsilon_\phi$ within their continuum ring width (or an increase within gap widths), we conclude that the dust gaps and rings coincide with the pressure minima and maxima, respectively. We then characterize these $\delta\upsilon_\phi$ substructures and report their properties in Table 1 following the procedure outlined in Section 3.4. We further comment on the $\delta\upsilon_\phi$ substructures that, although colocated with continuum substructures, do not align with the theoretical expectation of pressure maxima/minima, or could not be assessed due to limited angular resolution in Table 2 of Appendix A. The latter substructures are not included in the total count of nonaligning $\delta\upsilon_\phi$ substructures considered. We find that for ^{12}CO, 16 out of 21 continuum rings and 10 out of 12 continuum gaps align with negative and positive $\partial\delta\upsilon_\phi/\partial R$, respectively. In the case of ^{13}CO, $\partial\delta\upsilon_\phi/\partial R$ is negative for 14 out of 17 rings and positive for 8 out of 10 gaps. Therefore, more than 75% of dust continuum rings and 80% of gaps in both ^{12}CO and ^{13}CO coincide with local maxima and minima in the gas pressure. We emphasize that these pressure substructures identified through $\delta\upsilon_\phi$ variations in gas kinematics are reflected in the line centroids, not in the line *intensities*. Annotated $\delta\upsilon_\phi$ profiles highlighting the reported substructures listed in Table 1 can be found in Figures E5 and E6 of Appendix E.

Looking at large-scale $\delta\upsilon_\phi$ variations in Figure 4, most of the $R_{\mathrm{dust,95}}$ coincide with negative radial $\delta\upsilon_\phi$-gradients in ^{12}CO (13 out of 15), which hints toward radial inward drift of dust particles, i.e., the dust extent is shrinking. On the other hand, for HD 143006 and V4046 Sgr the gradient is positive in both tracers, which could point to colocation with a local pressure bump, i.e., a more stable dust outer edge. However, the ^{13}CO velocities, expected to be better tracers of the dust distribution near the midplane, show fewer negative slopes (only 7 out of 15; see Figure E3). This leads to ambiguity in some disks between ^{12}CO and ^{13}CO, where either slopes are decreasing or increasing, which will be further discussed in Section 6.4. In the outermost disk, beyond the continuum, $\delta\upsilon_\phi$ is radially decreasing within the outermost beam, i.e., $\partial\delta\upsilon_\phi/\partial R$ has a negative sign, for 10 out of 15 disks for ^{12}CO and 8 out of 15 disks for ^{13}CO. This result indicates that the gas temperature and/or density, and with it the pressure, is decreasing at these radii for over half of the sample.

6. Discussion

In this section, we discuss the accuracy and precision of our results and their implications. First, we investigate the robustness of the pressure variations and derive the midplane pressure derivative for a subset of our sample, a quantity of central importance for dust evolution. Second, we look at the uncertainties, systematics, and biases in determining azimuthal velocities from molecular line observations. Lastly, we will place our results into the bigger picture and compare our findings to predictions from theory.

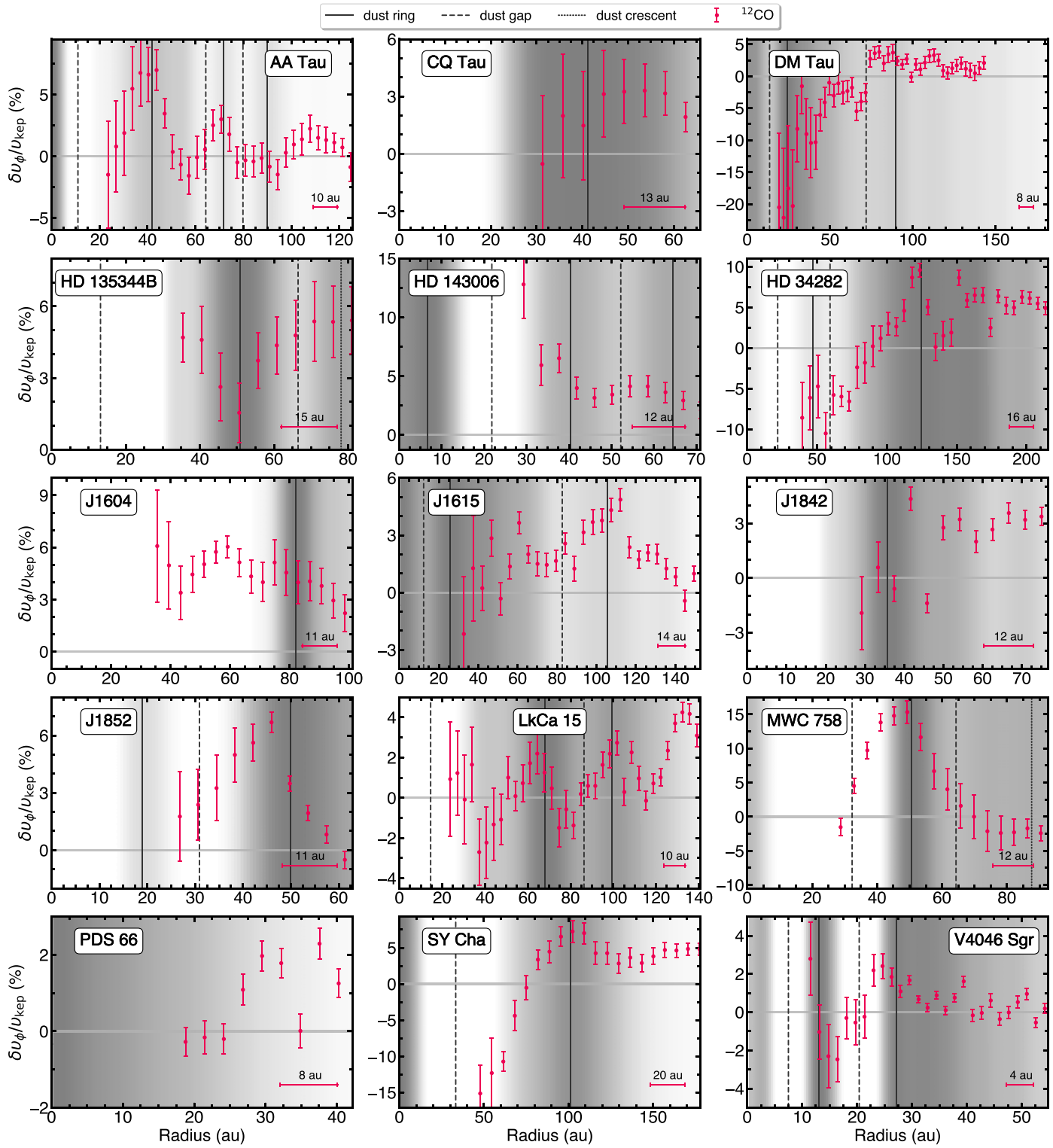

Figure 5. Radial profiles of δv_ϕ for ^{12}CO $J = 3$–2 of all sources focused on the region of the continuum substructures, using the high-resolution images. The profiles are plotted starting at two beam sizes from the disk center, and the error bars show the standard deviation of each bin. The gray background gradient highlights the `frank` radial profiles of the dust continuum emission normalized to its peak. The locations of continuum rings, gaps, and crescents are plotted in solid, dashed, and dotted vertical gray lines, respectively (P. Curone et al. 2025). We expect dust rings and gaps to be colocated with a decreasing and increasing δv_ϕ profile if caused by pressure maxima and minima, respectively. The beam size is plotted in the lower-right corner. The ^{13}CO δv_ϕ radial profiles can be found in Figure E4 of Appendix E.

6.1. Derivation of Midplane Pressure Derivative

In this section, we discuss the role of the pressure gradient in generating observed substructures in the dust continuum. Early theoretical studies have shown that the (midplane) gas pressure derivative determines the overall evolution of large dust grains in disks, as it sets their drift rate (F. L. Whipple 1972; S. J. Weidenschilling 1977). While the observed dust continuum is emitted close to the disk midplane, as millimeter

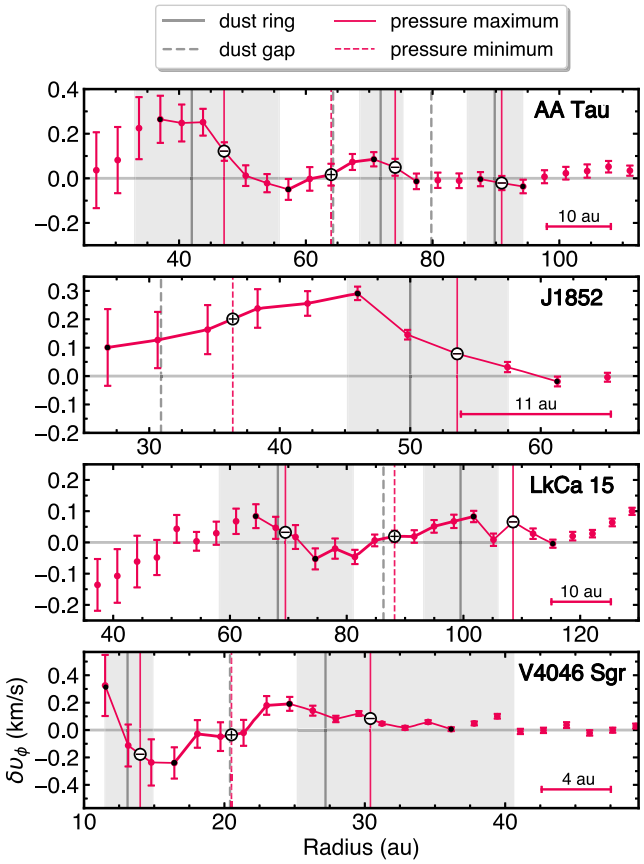

Figure 6. ^{12}CO δv_ϕ profiles for selected sources focused on the region of the continuum emission with highlighted radial locations of pressure substructures (red vertical lines). From Figure 1, we expect dust rings and gaps to be colocated with negative (⊖) and positive (⊕) δv_ϕ gradients if caused by pressure maxima and minima, respectively. The vertical gray shaded areas show the width of the continuum rings (P. Curone et al. 2025). The other plot annotations are the same as in Figure 5.

dust pebbles quickly settle (C. P. Dullemond & C. Dominik 2004; M. Villenave et al. 2020), CO molecular lines usually trace heights of $z/R \approx 0.2$–0.3 (e.g., C. J. Law et al. 2021; C. J. Law et al. 2023; M. Galloway-Sprietsma et al. 2025).

Given the vertical and radial thermal structure, defined by $c_s(R, z)$, as estimated by M. Galloway-Sprietsma et al. (2025) for a subset of our sample, we can overcome this spatial discrepancy and infer the midplane pressure gradient from the pressure gradient in the surface layers.

Following Appendix C, it can be shown that the slope of the midplane pressure profile is

$$\left.\frac{\partial \ln P}{\partial \ln R}\right|_{z=0} = \left.\frac{\partial \ln P}{\partial \ln R}\right|_{z=z_{\rm emit}} - \left.\frac{\partial \ln \chi}{\partial \ln R}\right|_{z=z_{\rm emit}}, \quad (12)$$

where $\chi(R, z)$ is given by

$$\chi(R, z) = \exp\left(-\int_{z=0}^{z} \frac{\Omega^2_{\rm k,mid}\, \tilde{z}}{c_s^2\,(R, \tilde{z})}\left[\frac{1}{1 + \tilde{z}^2/R^2}\right]^{3/2} {\rm d}\tilde{z}\right) \quad (13)$$

which is the ratio between the pressure at the emitting height z and the midplane.

In addition to the rotation curve, the derivations of the midplane pressure derivative require knowledge of the disk emission height, 2D temperature structure, and stellar mass. For the latter, we take the $M_\star$ estimates from C. Longarini et al. (2025) for the analysis presented in this section, since they simultaneously fit both CO rotation curves with a prescription for each term of Equation (1), which provides a more accurate estimate of $M_\star$ than the `discminer` kinematic stellar masses. However, since this procedure requires knowledge of the 2D temperature structure of the disk, it can only be employed on a subset of our sample. Because of this limitation, and for consistency, we remind the reader that in the rest of this Letter we have used the `discminer` kinematic stellar masses for our δv_ϕ analysis across the whole sample. To be consistent, we now also incorporate the C. Longarini et al. (2025)-derived self-gravity term into the subtraction of the background velocity (nominator Equation (9)) for sources that have nonnegligible disk masses ($M_{\rm disk} > 0.05 M_\star$), which are AA Tau, DM Tau, HD 34282, J1842, LkCa 15, and SY Cha. It is crucial to consider self-gravity in this context because it slightly increases the anticipated background velocity, by a few percent of the Keplerian speed (C. Longarini et al. 2025). This shift causes δv_ϕ to move to lower values, which is important to factor in as we are focusing on the points where δv_ϕ, and hence $\partial \ln {\rm P_{mid}}/\partial \ln {\rm R}$, intersect at zero.

We estimate the uncertainty of each parameter on $\partial \ln P_{\rm mid}/\partial \ln R$ via a Monte Carlo error propagation. We draw a total of 1000 samples, assuming Gaussian errors for the emission height (Equation (8)) and a 2D temperature structure (Equation (C12)) within the central 68% of the Markov Chain Monte Carlo posterior distribution of the model parameters (A. F. Izquierdo et al. 2025; M. Galloway-Sprietsma et al. 2025). However, the dominant uncertainty in the derivation of the midplane pressure profile is the stellar mass that determines the background Keplerian velocity. Even though only a few percent of uncertainty in $M_\star$ is enough to dominate over the combined uncertainty of the other parameters, it generally only changes δv_ϕ by a constant everywhere, therefore not altering the shape of the rotation curve. Still, some (small) variations in the shape of the rotation curve may result from systematic uncertainties in the multilevel fitting procedure. A rigorous treatment of all the uncertainties and covariances between them remains challenging. Applying such a comprehensive framework for error propagation to our data is beyond the scope of this Letter (see S. M. Andrews et al. 2024 for a detailed study). In our results, we neglect the combined bootstrapped uncertainties from the other parameters and only display the uncertainty of $M_\star$ on the pressure profiles. We vary $M_\star \pm \delta M_\star$ with $\delta M_\star = 3\%$, which is the precision currently achievable with the applied rotation curve fitting procedures (S. M. Andrews et al. 2024; B. Veronesi et al. 2024).

We present the profiles of the logarithmic radial derivative of the midplane pressure for the disks of J1615, LkCa 15, and V4046 Sgr in Figure 7. We chose to present these disks since their profiles show $\partial \ln {\rm P_{mid}}/\partial \ln {\rm R} = 0$ spatially coinciding with the location of the dust substructures within their uncertainties. However, this is not the case for all the disks and dust substructures, which will be discussed in the next section. In Appendix E, we present a gallery for the whole subsample in Figures E7 and E8.

We also made use of the 2D temperature structure and Equations (9) and (12) to assess the influence of the vertical temperature and pressure gradient on the slopes of our $\partial \delta v_\phi/\partial R$ profiles (Section 5.2) when projecting δv_ϕ to the midplane. The slope did not change significantly within the given uncertainties, hence we can state that the analysis of

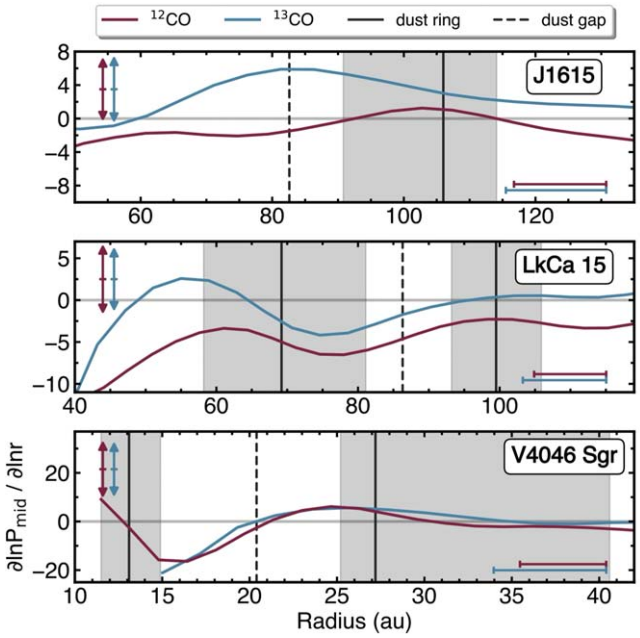

Figure 7. Radial profiles of $\partial \ln P_{\rm mid}/\partial \ln {\rm R}$ for selected sources, focused on the region of their continuum substructures. The vertical colored arrows in the upper left show variations in the stellar mass of ±3%, which would result in a shift of the whole profiles up and down. We expect dust rings and gaps to be colocated with $\partial \ln P_{\rm mid}/\partial \ln R = 0$ if induced by pressure maxima and minima (see Figure 1(b)). The vertical gray shaded areas show the width of the continuum rings (P. Curone et al. 2025). The other plot annotations are the same as in Figure 5.

pressure substructures using $\partial \delta v_\phi/\partial R$ at the emitting height is robust to infer the underlying pressure substructures.

6.2. Origins of Pressure Variations

Until now, we have remained agnostic on the origins of the substructures in δv_ϕ caused by underlying variations in pressure. In Section 5.1, we report that the majority of dust rings and gaps are colocated with corresponding maxima or minima in the gas pressure traced by $\partial \delta v_\phi/\partial R$. The question remains whether those pressure substructures are mainly driven by changes in the local gas temperature or density. In the latter case, one can imagine gas gaps that are carved out by planets (e.g., K. D. Kanagawa et al. 2015; R. Teague et al. 2018a) or gas density substructures caused by other mechanisms like self-induced dust traps, dead zones, the vertical shear instability, or magnetically driven winds (see J. Bae et al. 2023; G. Lesur et al. 2023 for a review). On the other hand, it has also been shown that strong radial gradients in temperature can lead to deviations from Keplerian rotation (M. Keppler et al. 2019; C. Rab et al. 2020).

We can disentangle the two contributions to the pressure by comparing the positive δv_ϕ gradients with the line width and peak brightness temperature radial profiles at these locations. In the presence of gas density gaps, we expect a local line-width minimum compared to the unperturbed background emission, when traced by the optically thick CO lines. Their broadened line widths are dominated by the density of the species rather than the temperature or turbulence, which is the case for optically thin emission (A. Hacar et al. 2016; A. F. Izquierdo et al. 2021). Hence, when simultaneously detecting a positive δv_ϕ gradient and a minimum in the line width with a high (nondecreasing) gas temperature, A. F. Izquierdo et al. (2023) shows that the deviation from Keplerian rotation is the result of a surface density dip. Conversely, if the increased temperature of the gas gap would be the driving mechanism, δv_ϕ would be expected to show a negative radial gradient, as has been studied by C. Rab et al. (2020).

In Figures E9 and E10 of Appendix E, we show the line-width residuals and peak intensity profiles for both CO molecules and all disks focused on the region of the continuum emission. Out of 17 continuum gaps with a positive CO δv_ϕ radial gradient, we identify nine that show a minimum in line widths, together with a warm gas temperature in either one or both of the CO molecules. This supports the interpretation of these pressure gaps being caused by surface density minima. In column (8) of Table 1, we highlight the gap substructures identified to be gas surface density gaps. We further give a rough estimate of planet masses potentially driving the δv_ϕ gap substructures in Appendix B using the relations derived in H.-G. Yun et al. (2019).

We can also see clear evidence of gas density cavities in the disks of CQ Tau, J1604, J1852, and MWC 758, as in those inner regions $\partial \delta v_\phi/\partial R$ is positive, coinciding with a line-width decrement and an increased peak intensity. Conversely, if the pressure gradient were dominated by strong changes in the disk temperature, we would expect $\partial \delta v_\phi/\partial R$ to be decreasing (e.g., C. Rab et al. 2020). The ^{13}CO rotation curves are expected to be more trustworthy in this analysis since their emission originates closer to the midplane and is more sensitive to variations in density rather than temperature, which is the case for ^{12}CO. A good example is J1604, where δv_ϕ is radially decreasing in ^{12}CO, though increasing for ^{13}CO.

In the case of dust continuum rings, we observe that approximately 75% of them are located alongside pressure bumps. However, the remaining rings do not exhibit a noticeable increase (or even a decrease) in the radial gradient of δv_ϕ or $\partial \ln P_{\rm mid}/\partial \ln R$ at their continuum peak location. This suggests that the underlying pressure structure may not be the exclusive cause of these rings. As discussed in Section 6.3, there might be shortcomings in the accurate measurement of v_ϕ at these close-in radial locations due to limited angular resolution. Some studies also show that dust rings can be produced without an underlying (static) pressure bump. Examples include ice lines (e.g., E. Saito & S.-i. Sirono 2011; K. Zhang et al. 2015; R. Hyodo et al. 2019), second-generation dust rings caused by the collisions of planetesimal rings (e.g., H. Jiang & C. W. Ormel 2021; L. Testi et al. 2022), or transient features in the gas surface density such as zonal flows (e.g., A. L. Uribe et al. 2011; M. Flock et al. 2015; C. Cui & X.-N. Bai 2021; C.-Y. Hsu et al. 2024). In the latter, magnetohydrodynamical simulations exhibit dust rings that no longer coincide with a pressure maximum that generated them, given the slow diffusion timescale of the rings in the case of low levels of turbulence (A. Riols & G. Lesur 2019).

The formation of continuum substructures is determined by the dynamics of the dust, which depends on the particle Stokes number and gas density. Consequently, one can also create dust rings through dust traffic jams (e.g., C. P. Dullemond & A. B. T. Penzlin 2018), a coagulation front of pebbles (e.g., S. Ohashi et al. 2021), or the dust back-reaction on the gas (e.g., H. Jiang & C. W. Ormel 2023). The morphology of substructures can also depend on the grain size distribution,

which will be investigated in a forthcoming paper by A. J. Winter et al. (2025, in preparation).

Lastly, the detection of kinematical substructures potentially driven by variations in gas pressure, extending well beyond the dust continuum emission, is intriguing (see Figure 4). It is often suggested that the outermost gas pressure substructure(s) set the outer-disk dust radius (P. Pinilla et al. 2020; A. Zormpas et al. 2022), raising questions on the dust trapping efficiency of the gas substructures seen beyond $R_{\rm dust,95}$ or/and the detectability of dust trapped therein. Low dust trapping efficiency for millimeter dust particles can happen if the *gas* surface density in the outermost regions is low ($St \gg 1$, $St \propto \Sigma_{\rm gas}^{-1}$), possibly resulting in low surface brightness, below detection limits. Dust diffusion is another possible explanation. This occurs for high values of α/St, such that the dust traps are leaky and cannot retain small micron-sized grains (e.g., for $St \ll 1$ and high α; see C. P. Dullemond et al. 2018; G. P. Rosotti et al. 2020). Additionally, the global pressure gradient may still be negative (as seen for most disks in Figure E8) such that the pressure substructures do not act as dust traps but only slow down the particle drift. Another possibility is that these pressure variations are short-lived and that those detected in the outer disk would have appeared after all the dust had drifted toward the inner disk. However, dynamic pressure bumps that appear and disappear over finite lifetimes—similar to zonal flows—are ineffective at preventing dust drift/loss over million-year timescales (e.g., J. Stadler et al. 2022).

6.3. How Well Can We Measure the Rotational Velocity?

The measurement of the gas velocity in protoplanetary disks requires knowledge of the geometry of the disk, such as its center, position angle, inclination, and emission height of the molecular line. Once these parameters are retrieved via fitting of kinematical data, it is possible to project a grid onto the line-of-sight velocity centroid map to determine the azimuthal velocity within each projected radial annulus. The procedure assumes that the azimuthal velocity is axisymmetric along the disk minor axis and that it dominates over radial and vertical motions in the line-of-sight velocity (Equation (2)). The latter statement safely holds for intermediate and high inclinations (i.e., $i \approx 30°$–$60°$), as the Keplerian rotation is approximately $\upsilon_{\rm kep} \approx 3.0\ {\rm km\ s^{-1}} \sqrt{M_\star/M_\odot} \sqrt{100\ {\rm au}/R}$. Meanwhile, the sound speed only reaches $c_s \approx 300\ {\rm m\ s^{-1}} \sqrt{T_{\rm gas}/25\ {\rm K}}$, providing an estimate of the magnitude of vertical and radial motions in the disk.

Still, it is possible to misinterpret velocity components due to problems in their decomposition. In particular, mistaking radial as azimuthal velocities and vice versa, due to nonaxisymmetric kinematical features. The most obvious case would be for a protoplanet embedded in a disk that excite spiral density waves launched at the Lindblad resonances (P. Goldreich & S. Tremaine 1979, 1980; J. Goodman & R. R. Rafikov 2001; R. R. Rafikov 2002) with associated nonaxisymmetric (radial) velocity perturbations (F. Bollati et al. 2021; D. Fasano et al. 2024). In Appendix D, we present a parameter study on the extraction of υ_ϕ from a hydrodynamical simulation with an embedded planet. We show that the misinterpretation of line-of-sight components further depends on the azimuthal location of the planet in the disk, as can be seen in Figure D1. It is the strongest if the planet is located right in between the minor and major axes of the disk, and the deviations from the *true* $\delta\upsilon_\phi$ velocity can be as big as 25%. This is as expected, since at these azimuths both υ_ϕ and $\upsilon_{\rm r}$ contribute strongly to the $\upsilon_{\rm los}$ (Equations (3) and (4)). Reassuringly, the shape of the $\delta\upsilon_\phi$ profile is hardly affected by this projection effect, hence the location of the inferred velocity and pressure substructures remain the same.

Another uncertainty in the extraction of azimuthal velocities lies in the retrieval of the stellar mass and disk inclination (S. M. Andrews et al. 2024). The inclination is important for the extraction of υ_ϕ itself, while the stellar mass only gets introduced in $\delta\upsilon_\phi$. For face-on disks, it can be hard to break the degeneracy of $M_\star \cdot \sin i$, which sometimes requires fixing the inclination to the value of the continuum. Nevertheless, for mid and high inclinations, the parameters can be robustly disentangled, and compare well to stellar masses reported in the literature (C. Longarini et al. 2025).

Lastly, there can be biases in determining the rotational velocity through a shift of the line centroid within one beam introduced by strong gradients in intensity. Such gradients can be of either a physical nature, like deep gas cavities in transition disks, or due to insufficient angular resolution. In the latter case, we expect to retrieve sub-Keplerian motion if the intensity gradient becomes too steep within one beam, most apparent in the inner regions of disks (either radially increasing or decreasing), so the centroid is shifted toward higher intensities (M. Keppler et al. 2019; Y. Boehler et al. 2021; S. M. Andrews et al. 2024). The same intensity shift occurs in the outermost regions of the disk, where the intensity diminishes and the SNR is low. In these areas, the CLEAN algorithm has difficulty capturing low-intensity diffuse emissions. The resulting noisy images can bias the estimates of location and velocity, causing the centroid to shift radially inward and leading to the retrieval of super-Keplerian rotation curves. Continuum subtraction (as applied on the cubes used in this work) can also affect the slope of the intensity profiles, but has been shown not to affect the retrieval of rotational velocities significantly (e.g., R. Teague et al. 2018a; A. F. Izquierdo et al. 2023).

6.4. Velocity Offsets between Molecular Lines

In this last section, we address the offset of $\delta\upsilon_\phi$ substructures as traced by ^{12}CO and ^{13}CO. We expect disks to be vertically stratified, i.e., to show a warmer upper disk layer and get cooler toward the midplane, as seen in observations (C. J. Law et al. 2021; M. Galloway-Sprietsma et al. 2025). Therefore, the thermal pressure gradient is different at distinct heights in the disk, which leads to the differences of rotation between ^{12}CO and ^{13}CO shown in Section 4.1. Yet, there appears to be a dependency with radius on the level of vertical velocity stratification traced via the differences in rotation of ^{12}CO and ^{13}CO. Vertical stratification appears more pronounced at larger radii than smaller ones, thus radially more extended sources show a higher degree of stratification than smaller ones. The exceptions are the highly dynamically perturbed and small ($r < 150$ au) stratified disks of CQ Tau and MWC 758, and the extended but very smooth nonstratified disk of V4046.

We see that, particularly at large radii, ^{12}CO and ^{13}CO exhibit big differences in emission heights. In contrast, at short separations, the emission surfaces are located close to each other (see Figure 5 in M. Galloway-Sprietsma et al. 2025). In other words, ^{12}CO and ^{13}CO trace very distinct disk regions in temperature and density at large orbital radii, leading to substantial differences in their pressure gradient and rotation.

This effect has recently been studied in detail by V. Pezzotta et al. (2025) and explains the vertical stratification observed at large distances for extended sources. It also clarifies why V4046 lacks any vertical stratification, as here the ^{12}CO and ^{13}CO emission surfaces do trace similar heights and thus pressure gradients throughout the disk (M. Galloway-Sprietsma et al. 2025; A. F. Izquierdo et al. 2025). The different vertical and radial temperature gradients between the CO molecules can also help to explain their different gradients in δv_ϕ. It has been shown that strong radial temperature gradients can lead to beam-smearing effects and thus artificial δv_ϕ variations (M. Keppler et al. 2019; A. J. Bohn et al. 2022; V. Pezzotta et al. 2025). For a few sources, we observe opposing δv_ϕ gradients between ^{12}CO and ^{13}CO extending no more than 100 au in radius in the outer-disk regions (see AA Tau, DM Tau, and J1615 in Figure E11). The peak intensity radial profiles show a *negative* temperature gradient at those radii in both lines (see Figure 3 in M. Galloway-Sprietsma et al. 2025), which should result in a *positive* δv_ϕ gradient if driven by the temperature variation in both lines. This is observed in ^{12}CO for AA Tau ($R \sim 200$–300 au) and J1615 ($R \sim 400$–480 au), however not in their ^{13}CO curves.

Another possibility for the δv_ϕ mismatch is that not all disks are in centrifugal balance or vertical hydrostatic equilibrium in their respective layers, i.e., there are nonnegligible asymmetric vertical and radial velocity flows, which can introduce mismeasurement of v_ϕ between the lines at those regions of interest. The predominantly negative midplane pressure derivatives (see Figure E7) indicate steep pressure profiles, in particular for the transition disks of HD 34282 and SY Cha, which are indicative of a centrifugal imbalance. Potentially, there could be fast (several hundreds of meters per second) radial flows at these cavity edges (e.g., J. Calcino et al. 2025), hence the gas disk expands outwards, thus not being in centrifugal equilibrium. Another possibility is that such steep pressure profiles are signposts of the Rossby wave instability that has been shown to produce such features and vortices (e.g., H. Meheut et al. 2010; E. Chang et al. 2023). This is potentially traced in the three most asymmetric continuum disks in our sample, HD 135344B, HD 143006, and MWC 758, which all exhibit continuum crescents (P. Curone et al. 2025; L. Wölfer et al. 2025). Due to incomplete determination of the vertical physical structure, we could not derive their $\partial \ln P_{mid}/\partial \ln R$ profiles, though their δv_ϕ profiles show negative gradients colocated with their dust continuum crescents indicative of pressure bumps (see Figure 5).

7. Conclusions

In this sixth Letter of the exoALMA series, we presented the rotation curves and deviations from Keplerian rotation (δv_ϕ) of the ^{12}CO $J = 3$–2 and ^{13}CO $J = 3$–2 line emission for the entire exoALMA sample.

(i) We show that the CO rotational velocities show clear evidence of vertical stratification, i.e., the ^{13}CO molecular line rotates faster than the ^{12}CO line. This mismatch in rotation cannot be explained by differences in gravity and a constant temperature alone, indicating that the thermal pressure gradient differs at distinct heights in the disk, which is expected for disks with a hot surface layer and a cold midplane.

(ii) Substructures in δv_ϕ are ubiquitous in our sample, both on small ($\sim$10 au) and large ($\sim$100 au) radial scales, indicative of strong pressure variations driving them. We also observe pressure substructures well beyond the dust continuum emission, superimposed on the overall steep pressure drop at the farthest radii. This raises the question of why the dust is not trapped by these substructures in the outer disk.

(iii) We observe that a majority of continuum rings (75%) and gaps (80%) are colocated with gas pressure maxima and minima, respectively, as traced by the radial derivative of δv_ϕ of the CO molecular lines. We emphasize that these kinematic signatures are not manifested in the line *intensities*, solely in the line centroid. Hence, we conclude that variations in gas pressure are likely the dominant mechanism for ring and gap formation in the dust continuum.

(iv) Positive δv_ϕ radial gradients indicate variation in the gas density rather than temperature, indicating the presence of gas surface density gaps colocated with continuum gaps, potentially carved out by embedded protoplanets.

(v) On large scales, we find most disks to rotate at sub-Keplerian speeds due to a negative pressure gradient induced by the drop in gas density and temperature at these outer radii. This has profound impacts on dust dynamics since it increases the radial inward drift of pebbles in the outer-disk regions. This could rapidly replenish and enrich the inner disk with dust from the outer domains.

(vi) For the first time, we determine the midplane gas pressure derivative from observational data. For a few sources we find that $\partial \ln P_{mid}/\partial \ln R = 0$ is colocated with continuum substructures, confirming the presence of underlying gas pressure bumps as predicted by theory (e.g., S. J. Weidenschilling 1977; T. Birnstiel et al. 2010).

(vii) The data presented in this Letter are publicly released as a value-added data product (VADP). The VADP release includes the radial profiles of rotation curves v_ϕ, the Keplerian background rotation v_k, deviations from Keplerian rotation δv_ϕ, and the midplane pressure derivative for all three sets of continuum-subtracted image cubes. The properties of the reported δv_ϕ substructures listed in Table 1 will also be included in the release.

In conclusion, this Letter demonstrates that the study of rotational velocities traced via high-angular-resolution molecular line ALMA observations opens a unique window to comprehensively analyze the underlying dynamical and gas pressure substructures of planet-forming disks. Future work investigating the properties and abundance of these substructures will help us to further unravel their physical nature, bringing us a step closer in our pursuit to detect protoplanets in formation.

Acknowledgments

The authors would like to thank the anonymous referee for the thoughtful and constructive feedback, which significantly improved the quality of this work, as well as Haochang Jiang, Bin Ren, Viviana Pezzotta, and Richard Booth for their helpful discussions. This Letter makes use of the following ALMA data: ADS/JAO.ALMA#2021.1.01123.L. ALMA is a partnership of

ESO (representing its member states), NSF (USA) and NINS (Japan), together with NRC (Canada), MOST and ASIAA (Taiwan), and KASI (Republic of Korea), in cooperation with the Republic of Chile. The Joint ALMA Observatory is operated by ESO, AUI/NRAO, and NAOJ. The National Radio Astronomy Observatory is a facility of the National Science Foundation operated under cooperative agreement by Associated Universities, Inc. We thank the North American ALMA Science Center (NAASC) for their generous support, including providing computing facilities and financial support for student attendance at workshops and publications.

J.S., M.B., and D.F. have received funding from the European Research Council (ERC) under the European Union's Horizon 2020 research and innovation programme (PROTOPLANETS, grant agreement No. 101002188). J.S. has performed computations on the "Mesocentre SIGAMM" machine, hosted by Observatoire de la Cote d'Azur. A.J.W. has received funding from the European Union's Horizon 2020 research and innovation programme under the Marie Skłodowska-Curie grant agreement No 101104656. Support for A. F.I. was provided by NASA through a NASA Hubble Fellowship, grant No. HST-HF2-51532.001-A, awarded by the Space Telescope Science Institute, which is operated by the Association of Universities for Research in Astronomy, Inc., for NASA, under contract NAS5-26555. C.L. has received funding from the European Union's Horizon 2020 research and innovation program under the Marie Sklodowska-Curie grant agreement No. 823823 (DUSTBUSTERS) and by the UK Science and Technology research Council (STFC) via the consolidated grant No. ST/W000997/1. P.C. acknowledges support by the Italian Ministero dell'Istruzione, Università e Ricerca, through the grant Progetti Premiali 2012—iALMA (CUP C52I13000140001) and by the ANID BASAL project FB210003. J.B. acknowledges support from NASA XRP grant No. 80NSSC23K1312. N.C. has received funding from the European Research Council (ERC) under the European Union Horizon Europe research and innovation program (grant agreement No. 101042275, project Stellar-MADE). S.F. is funded by the European Union (ERC, UNVEIL, 101076613), and acknowledges the financial contribution from PRIN-MUR 2022YP5ACE. M.F. is supported by a Grant-in-Aid from the Japan Society for the Promotion of Science (KAKENHI, grant No. JP22H01274). C.H. acknowledges support from NSF AAG grant No. 2407679. I.H. acknowledges a Research Training Program scholarship from the Australian Government. T.H. is supported by an Australian Government Research Training Program (RTP) Scholarship. J.D.I. acknowledges support from an STFC Ernest Rutherford Fellowship (grant No. ST/W004119/1) and a University Academic Fellowship from the University of Leeds. G.L. has received funding from the European Union's Horizon 2020 research and innovation program under the Marie Sklodowska-Curie grant agreement No. 823823 (DUSTBUSTERS). F.M. has received funding from the European Research Council (ERC) under the European Union's Horizon Europe research and innovation program (grant agreement No. 101053020, project Dust2Planets). C.P. acknowledges Australian Research Council funding via grant Nos. FT170100040, DP18010423, DP220103767, and DP240103290. D.P. acknowledges Australian Research Council funding via grant Nos. DP18010423, DP220103767, and DP240103290. G.R. acknowledges funding from the Fondazione Cariplo, grant No. 2022-1217, and the European Research Council (ERC) under the European Union's Horizon Europe Research & Innovation Programme under grant agreement No. 101039651 (DiscEvol). H.-W.Y. acknowledges support from the National Science and Technology Council (NSTC) in Taiwan through grant No. NSTC 113-2112-M-001-035- and from an Academia Sinica Career Development Award (grant No. AS-CDA-111-M03). G.W.F. acknowledges support from the European Research Council (ERC) under the European Union Horizon 2020 research and innovation program (grant agreement No. 815559, MHDiscs). G.W.F. was granted access to the HPC resources of IDRIS under the allocation A0120402231 made by GENCI. T.C.Y. acknowledges support by a Grant-in-Aid for JSPS Fellows (grant No. JP23KJ1008). Support for B.Z. was provided by The Brinson Foundation. Views and opinions expressed by ERC-funded scientists are however those of the author(s) only and do not necessarily reflect those of the European Union or the European Research Council. Neither the European Union nor the granting authority can be held responsible for them.

Software: Astropy (Astropy Collaboration et al. 2022), CARTA (A. Comrie et al. 2021), CASA (CASA Team et al. 2022), Discminer (A. F. Izquierdo et al. 2021), Eddy (R. Teague 2019), Grammarly (https://www.grammarly.com/; last used 01/2025), Matplotlib (J. D. Hunter 2007), NumPy (S. van der Walt et al. 2011), SciPy (P. Virtanen et al. 2020).

Appendix A
Substructures

Table 1 provides the properties of δv_ϕ pressure-substructures co-located with the continuum gaps and rings, measured as outlined in Section 3.4. We comment on continuum substructures that do not align with the expected δv_ϕ variations in Table 2.

Table 1
Properties of the $\delta v\phi$ Substructures Collocated with Continuum Gaps and Rings

Source	Feature	Tracer	Radial Location (au, mas)	Width (au, mas)	Amplitude (m/s, % vk, M_{jup})	Offset (au, m/s)	Σ_{gap}	Comments
DM Tau	D72	^{12}CO	73 ± 4, 506 ± 29	14 ± 4, 95 ± 29	213 ± 40, 9.4, **1.2**	1, -25	O	⋯
	B90	^{12}CO	94 ± 4, 649 ± 29	11 ± 4, 76 ± 29	78 ± 30, 3.9	4, 37	⋯	⋯
		^{13}CO	91 ± 4, 630 ± 29	17 ± 4, 120 ± 29	96 ± 24, 4.5	1, -39	⋯	⋯
AA Tau	B42	^{12}CO	47 ± 5, 350 ± 37	20 ± 5, 150 ± 37	314 ± 116, 9.1	5, 107	⋯	⋯
		^{13}CO	44 ± 6, 330 ± 45	8 ± 6, 60 ± 45	237 ± 105, 6.3	2, -15	⋯	Width < one beam size
	D64	^{12}CO	64 ± 5, 475 ± 37	13 ± 5, 100 ± 37	135 ± 57, 4.5, **0.4**	-0, 18	✓	⋯
		^{13}CO	63 ± 6, 465 ± 45	12 ± 6, 90 ± 45	107 ± 43, 3.4	-2, -34	✓	⋯
	B72	^{12}CO	74 ± 5, 550 ± 37	7 ± 5, 50 ± 37	99 ± 47, 3.6	2, 36	⋯	Width < one beam size
		^{13}CO	73 ± 6, 540 ± 45	8 ± 6, 60 ± 45	61 ± 50, 2.1	1, -11	⋯	Width < one beam size
	D80	^{13}CO	81 ± 6, 600 ± 45	8 ± 6, 60 ± 45	95 ± 56, 3.4, **0.3**	1, 6	O	Width < one beam size
	B90	^{12}CO	91 ± 5, 675 ± 37	7 ± 5, 50 ± 37	33 ± 44, 1.3	1, -20	⋯	Width < one beam size
		^{13}CO	95 ± 6, 705 ± 45	20 ± 6, 150 ± 45	81 ± 46, 3.1	5, 13	⋯	Center outside of ring Width
LkCa 15	B68	^{12}CO	70 ± 5, 442 ± 32	10 ± 5, 65 ± 32	137 ± 51, 3.7	1, 16	⋯	⋯
		^{13}CO	69 ± 6, 437 ± 37	12 ± 6, 75 ± 37	237 ± 36, 6.3	1, -1	⋯	⋯
	D86	^{12}CO	88 ± 5, 561 ± 32	27 ± 5, 173 ± 32	136 ± 38, 4.2, **0.7**	2, 15	O	⋯
		^{13}CO	82 ± 6, 525 ± 37	16 ± 6, 100 ± 37	142 ± 33, 4.1, **0.7**	-4, -49	✓	⋯
	B100	^{12}CO	109 ± 5, 690 ± 32	14 ± 5, 86 ± 32	87 ± 22, 3.0	9, 39	⋯	Center outside of ring width
HD 34282	D59	^{12}CO	90 ± 8, 291 ± 27	67 ± 8, 218 ± 27	788 ± 123, 21.5	31, -97	✓	⋯
		^{13}CO	85 ± 12, 275 ± 37	46 ± 12, 150 ± 37	609 ± 271, 15.4	26, -104	O	⋯
	B124	^{12}CO	129 ± 8, 418 ± 27	11 ± 8, 36 ± 27	293 ± 56, 9.7	5, 150	⋯	⋯
		^{13}CO	139 ± 12, 450 ± 37	62 ± 12, 200 ± 37	202 ± 83, 6.5	15, 100	⋯	⋯
MWC 758	D32	^{12}CO	37 ± 6, 237 ± 40	16 ± 6, 105 ± 40	849 ± 105, 15.1	5, 327	✓	⋯
		^{13}CO	44 ± 7, 279 ± 47	19 ± 7, 124 ± 47	687 ± 142, 12.6	11, 4	(✓)	Cold density gap
	B51	^{12}CO	60 ± 6, 382 ± 40	29 ± 6, 185 ± 40	836 ± 136, 18.9	9, 333	⋯	Center outside of ring width
		^{13}CO	68 ± 7, 434 ± 47	29 ± 7, 186 ± 47	529 ± 92, 12.1	17, 83	⋯	Center outside of ring width
SY Cha	B101	^{12}CO	116 ± 10, 638 ± 56	27 ± 10, 150 ± 56	119 ± 49, 5.1	15, 123	⋯	⋯
		^{13}CO	102 ± 10, 562 ± 56	27 ± 10, 150 ± 56	122 ± 58, 4.5	1, -48	⋯	⋯
HD 135344B	B51	^{12}CO	43 ± 8, 319 ± 56	15 ± 8, 112 ± 56	215 ± 92, 3.8	-8, 189	⋯	⋯
		^{13}CO	43 ± 8, 319 ± 56	15 ± 8, 112 ± 56	154 ± 86, 2.6	-8, 152	⋯	⋯
	D66	^{12}CO	61 ± 8, 450 ± 56	20 ± 8, 150 ± 56	157 ± 99, 3.3	-6, 160	O	High amplitude uncertainty
		^{13}CO	61 ± 8, 450 ± 56	20 ± 8, 150 ± 56	58 ± 79, 1.2	-6, 105	O	High amplitude uncertainty
HD 143006	B40	^{12}CO	38 ± 6, 225 ± 37	17 ± 6, 100 ± 37	657 ± 189, 11.7	-3, 488	⋯	⋯
	B64	^{12}CO	65 ± 6, 387 ± 37	21 ± 6, 125 ± 37	136 ± 48, 3.2	0, 123	⋯	⋯
		^{13}CO	72 ± 9, 431 ± 56	19 ± 9, 112 ± 56	170 ± 42, 4.1	8, 53	⋯	Center outside of ring width
J1604	B82	^{12}CO	97 ± 6, 669 ± 41	36 ± 6, 246 ± 41	279 ± 62, 8.0	15, 35	⋯	Center outside of ring width
		^{13}CO	89 ± 8, 619 ± 56	49 ± 8, 338 ± 56	286 ± 45, 7.8	7, 46	⋯	Center outside of ring width
J1615	D83	^{12}CO	93 ± 7, 599 ± 45	37 ± 7, 239 ± 45	89 ± 28, 2.8, **0.6**	11, 95	✓	Center outside of gap width
		^{13}CO	66 ± 8, 423 ± 49	30 ± 8, 195 ± 49	200 ± 48, 5.1, **0.9**	-17, -13	✓	Center outside of gap width
	B106	^{13}CO	99 ± 8, 635 ± 49	36 ± 8, 228 ± 49	91 ± 29, 2.9	-7, 41	⋯	⋯
V4046 Sgr	B13	^{12}CO	14 ± 2, 195 ± 34	5 ± 2, 69 ± 34	566 ± 251, 5.4	1, 43	⋯	⋯
	D20	^{12}CO	21 ± 2, 287 ± 34	8 ± 2, 115 ± 34	431 ± 125, 5.0, **0.7**	0, -24	✓	⋯
		^{13}CO	19 ± 3, 270 ± 45	9 ± 3, 120 ± 45	434 ± 170, 4.8, **0.6**	-1, 4	O	⋯
	B27	^{12}CO	30 ± 2, 425 ± 34	12 ± 2, 161 ± 34	185 ± 53, 2.6	3, 99	⋯	⋯
		^{13}CO	33 ± 3, 465 ± 45	6 ± 3, 90 ± 45	175 ± 28, 2.6	6, 35	⋯	⋯
J1852	D31	^{12}CO	36 ± 6, 248 ± 39	19 ± 6, 130 ± 39	191 ± 137, 3.9, **0.6**	5, 196	✓	High amplitude uncertainty
	B50	^{12}CO	54 ± 6, 365 ± 39	15 ± 6, 104 ± 39	310 ± 29, 7.7	4, 136	⋯	⋯
		^{13}CO	58 ± 7, 393 ± 45	18 ± 7, 121 ± 45	129 ± 33, 3.3	8, 33	⋯	Center outside of ring width

Note. Column (1): target name sorted by their R.A. Column (2): annular substructure label as in P. Curone et al. (2025). "B" (for bright) indicates a ring, while "D" (for dark) indicates a gap. The number on the label is the feature distance from the central star measured in au. Column (3): observational tracer. Columns (4)-(6): $\delta v\phi$ substructure radial location, width, and amplitude inferred as explained in Sect. 3.4. Column (7): radial and velocity offset from the center of continuum substructure and $\delta v\phi$=0, respectively. Column (8): detection (✓) of a dip in line widths together with nondecreasing peak intensities at continuum gap location indicative of a co-located surface density gap Σ_{gap} as discussed in Sect. 6.2. No decrease in line width was detected for gap rows marked with "O". Column (9): comments regarding irregularities. Comments on $\delta v\phi$ substructures collocated with continuum substructures nonreported in this table can be found in Table 2 in the Appendix. The radial $\delta v\phi$ profile with annotated substructures reported in this table can be found in Figures E5 and E6.

Table 2
Comments to Nonreported $\delta v\phi$ at Continuum Substructures

Source	Feature	Tracer	Comments
DM Tau	D14	^{12}CO, ^{13}CO	Not accessible due to limited angular resolution
	B24	^{12}CO	Reversed (positive) $\delta v\phi$ gradient
	B24	^{13}CO	Not accessible due to limited angular resolution
	D72	^{13}CO	Reversed (negative) $\delta v\phi$ gradient
AA Tau	D11	^{12}CO, ^{13}CO	Not accessible due to limited angular resolution
	D80	^{12}CO	Flat $\delta v\phi$ profile
LkCa 15	D15	^{12}CO, ^{13}CO	Not accessible due to limited angular resolution
	B100	^{13}CO	Flat $\delta v\phi$ profile
HD 34282	D22	^{12}CO, ^{13}CO	Not accessible due to limited angular resolution
	B47	^{12}CO	Reversed (positive) $\delta v\phi$ gradient
	B47	^{13}CO	Not accessible due to limited angular resolution
MWC 758	D64, B88	^{12}CO, ^{13}CO	Asymmetric ring (vortex) with negative $\delta v\phi$ gradient
CQ Tau	B41	^{12}CO, ^{13}CO	Reversed and flat $\delta v\phi$ gradient, respectively
SY Cha	D33	^{12}CO, ^{13}CO	Not accessible due to limited angular resolution
HD 135344B	D13	^{12}CO, ^{13}CO	Not accessible due to limited angular resolution
	D66, B78	^{12}CO, ^{13}CO	Asymmetric ring (vortex) with negative $\delta v\phi$ gradient
HD 143006	B7, D22	^{12}CO, ^{13}CO	Not accessible due to limited angular resolution
	B40	^{13}CO	Reversed (positive) $\delta v\phi$ gradient
	D52	^{12}CO, ^{13}CO	Flat and reversed $\delta v\phi$ gradient, respectively
J1615	D12, B26	^{12}CO, ^{13}CO	Not accessible due to limited angular resolution
	B106	^{12}CO	Reversed (positive) $\delta v\phi$ gradient
V4046 Sgr	D8	^{12}CO, ^{13}CO	Not accessible due to limited angular resolution
	B13	^{13}CO	Not accessible due to limited angular resolution
J1842	B36	^{12}CO	Reversed (positive) $\delta v\phi$ gradient
	B36	^{13}CO	Not accessible due to limited angular resolution
J1852	B19	^{12}CO, ^{13}CO	Not accessible due to limited angular resolution
	D31	^{13}CO	Not accessible due to limited angular resolution

Note. Column (1): target name sorted by their R.A. Column (2): annular substructure label. "B" (for bright) indicates a ring, while "D" (for dark) indicates a gap. The number on the label is the feature distance from the central star measured in au. Column (3): Observational tracer of $\delta v\phi$. Column (4): Comments for why substructures were not reported. Note that dust substructures inaccessible due to limited angular resolution are not included in the total count of non-aligning $\delta v\phi$-substructures considered.

Appendix B
Planet Masses from δv_ϕ Perturbations

In this section, we provide rough estimates of planet masses that are potentially driving the δv_ϕ perturbations observed colocated with the dust continuum gaps reported in Table 1. To this end, we follow the approach of H.-G. Yun et al. (2019) that relates the gap width of the δv_ϕ perturbation to the planet mass via a set of 2D hydrodynamical simulations. We estimate the planet mass M_p by numerically solving their Equation (20):

$$\frac{W_v}{h_p} = 2.66\left(\frac{M_p}{M_{\rm th}}\right)^{-0.41} + 2.04\left(\frac{M_p}{M_{\rm th}}\right)^{0.42}, \tag{B1}$$

where W_v is the δv_ϕ gap width, h_p the pressure scale height at the planet's radial location r_p, and $M_{\rm th} \equiv M_\star(h_p/r_p)^3$ the thermal mass. The pressure scale is given via $h_p = c_{\rm s}\Omega_K$, where Ω_K is the Keplerian frequency. The sound speed $c_{\rm s}$ gets evaluated at the disk midplane using the midplane temperatures as measured in M. Galloway-Sprietsma et al. (2025; see Equation (C11)). For disks for which no 2D temperature profile could be measured, we estimate the midplane temperature via the expected irradiation temperature following M. Galloway-Sprietsma et al. (2025):

$$T_{\rm irr}(r) = \left(\frac{L_*}{8\pi R^2 \sigma_{\rm SB}}\right)^{1/4}, \tag{B2}$$

where L_* is the stellar luminosity, R is the distance from the central star, and $\sigma_{\rm SB}$ is the Stefan–Boltzmann constant (P. D'Alessio et al. 2001). We report the rough planet mass estimates following the above equations in Table 3.

Table 3
Planet Masses Derived from $\delta v\phi$ Gap Properties

Source	Feature	Tracer	Radial Location r_p (au)	Width W_v (au)	Pressure Scale Height $h_p(r_p)$ (au)	Planet Mass (M_{jup})
DM Tau	D72	^{12}CO	73 ± 4	14 ± 4	8.8	1.1
AA Tau	D64	^{12}CO	64 ± 5	13 ± 5	4.3	2.4
		^{13}CO	63 ± 6	12 ± 6	4.2	2.6
	D80	^{13}CO	81 ± 6	8 ± 6	5.9	0.44
LkCa 15	D86	^{12}CO	88 ± 5	27 ± 5	7.0	0.82
		^{13}CO	82 ± 6	16 ± 6	6.3	0.75
HD 34282	D59	^{12}CO	90 ± 8	67 ± 8	7.7	1.4
		^{13}CO	85 ± 12	46 ± 12	7.2	1.4
MWC 758	D32	^{12}CO	37 ± 6	16 ± 6	4.1[a]	2.7
		^{13}CO	44 ± 7	19 ± 7	5.0[a]	3.1
HD 135344B	D66	^{12}CO	61 ± 8	20 ± 8	6.0[a]	2.1
		^{13}CO	61 ± 8	20 ± 8	6.0[a]	2.2
J1615	D83	^{12}CO	93 ± 7	37 ± 7	8.3	1.1
		^{13}CO	66 ± 8	30 ± 8	5.2	2.5
V4046 Sgr	D20	^{12}CO	21 ± 2	8 ± 2	1.0	5.9
		^{13}CO	19 ± 3	9 ± 3	0.9	5.7
J1852	D31	^{12}CO	36 ± 6	19 ± 6	2.9	16[b]

Notes. Column (1): target name sorted by their R.A. Column (2): annular substructure label as in P. Curone et al. (2025), "D" (for *dark*) indicates a gap. The number on the label is the dust feature's distance from the central star measured in au. Column (3): observational tracer. Column (4+5): $\delta v\phi$ substructure radial location and width same as Table 1 inferred as explained in Sect. 3.4. Column (7): Gas pressure scale height at $\delta v\phi$ radial location computed using gas midplane temperatures from M. Galloway-Sprietsma et al. (2025). Column (8): Planet mass estimates in masses of Jupiter derived from the $\delta v\phi$ width using Eq. B1 as in H.-G. Yun et al. (2019). Radial $\delta v\phi$-profile with annotated substructures reported in this table can be found in Figures E5 & E6.
[a] Gas pressure scale height computed via stellar luminosity midplane irradiation using Equation (B2): MWC 758 ($L_\star = 20L_\odot$) and HD 135344B ($L_\star = 5.1L_\odot$) from V. Mannings & A. I. Sargent (2000) and J. Guzmán-Díaz et al. (2021), respectively.
[b] High planet mass estimate due to hot midplane temperature $T_{mid}(r_p) = 43$K (see Fig. 5 in M. Galloway-Sprietsma et al. 2025).

Appendix C
Derivation of the Radial Gradient of the Midplane Pressure

To quantify the pressure variations in the midplane, we first assume that the local disk at the cylindrical radius R is in vertical hydrostatic equilibrium such that

$$\left.\frac{\partial P}{\partial z}\right|_R = \left.\frac{\partial(\rho_{gas}c_s^2)}{\partial z}\right|_R = -\frac{GM_\star\rho_{gas}z}{(R^2+z^2)^{3/2}}. \quad \text{(C1)}$$

Here, we have already imposed a functional form for $c_s(R, z)$ such that the above equation can be directly integrated over z to yield the expression

$$\rho_{gas}(R, z) = \frac{\rho_0\,\chi}{g}, \quad \text{(C2)}$$

where

$$\chi(R, z) = \exp\left(-\int_0^z \frac{\Omega_{kep,mid}^2\,\tilde{z}}{c_s^2(\tilde{z})}\left[\frac{1}{1+\tilde{z}^2/R^2}\right]^{3/2} d\tilde{z}\right) \quad \text{(C3)}$$

and

$$g(R, z) = \frac{c_s^2}{c_{s,mid}^2} = \frac{T}{T_{mid}}. \quad \text{(C4)}$$

The radial pressure gradient at a given height z is

$$\left.\frac{\partial \ln P}{\partial \ln R}\right|_z = \frac{\partial \ln \rho_0}{\partial \ln R} + \frac{\partial \ln c_{s,mid}^2}{\partial \ln R} + \left.\frac{\partial \ln \chi}{\partial \ln R}\right|_z. \quad \text{(C5)}$$

The first two components on the right-hand side of Equation (C5) are

$$\frac{\partial \ln \rho_0}{\partial \ln R} = \frac{\partial \ln \Sigma_g}{\partial \ln R} - \frac{\partial \ln H}{\partial \ln R}, \quad \text{(C6)}$$

where

$$\frac{\partial \ln H}{\partial \ln R} = \frac{\partial \ln c_{s,mid}}{\partial \ln R} + \frac{3}{2}. \quad \text{(C7)}$$

The last component of Equation (C5) can be written

$$\frac{\partial \ln \chi}{\partial \ln R} = -\int_0^z \frac{f\tilde{z}}{gH^2}\left\{\frac{\partial \ln f}{\partial \ln R} - \frac{\partial \ln g}{\partial \ln R} - 2\frac{\partial \ln H}{\partial \ln R}\right\} d\tilde{z}, \quad \text{(C8)}$$

where we have defined

$$f(R, z) = \left(\frac{1}{1+z^2/R^2}\right)^{3/2}. \quad \text{(C9)}$$

So far, all of the components of Equation (C8) are general. Then, we assume a functional form for the temperature structure derived by E. Dartois et al. (2003) and fitted for in M. Galloway-Sprietsma et al. (2025), where the midplane temperature T_{atm} and atmospheric temperature T_{atm} are described by power laws:

$$T_{atm}(R) = T_{atm,p}(R/100\text{ au})^{-q_{atm}}, \quad \text{(C10)}$$

$$T_{mid}(R) = T_{mid,p}(R/100\text{ au})^{-q_{mid}}. \quad \text{(C11)}$$

At each radius and height between the atmosphere and midplane, the temperature is then smoothly connected using a squared cosine function: where Z_q is also given by a power law,

$$T(R, z) = \begin{cases} T_{\rm atm}(R) + [\, T_{\rm mid}(R) - T_{\rm atm}(R)] \cos^2\left(\frac{\pi}{2}\frac{z}{Z_q}\right) & \text{if } z < Z_q \\ T_{\rm atm}(R) & \text{if } z \geqslant Z_q, \end{cases} \tag{C12}$$

$Z_q(R) = Z_0(R/100\ \text{au})^{q_z}$. Then, the radial derivative of $g(R, z) = T/T_{\rm mid}$ is denoted by

$$\frac{\partial \ln g}{\partial \ln R} = \frac{\partial \ln T}{\partial \ln R} - \frac{\partial \ln T_{\rm mid}}{\partial \ln R}, \tag{C13}$$

where

$$\frac{\partial \ln T}{\partial \ln R} = \begin{cases} -\frac{1}{T}\left[q_{\rm atm} \cdot T_{\rm atm}\left(1 + \left(\frac{q_{\rm mid} T_{\rm mid}}{q_{\rm atm} T_{\rm atm}} - 1\right) \cdot \cos^2\left(\frac{\pi}{2}\frac{z}{Z_q}\right)\right) + \frac{\pi}{2}\frac{q_z \cdot z}{Z_q}(T_{\rm atm} - T_{\rm mid}) \sin\left(\pi \frac{z}{Z_q}\right)\right] & \text{if } z < Z_q \\ -q_{\rm atm} & \text{if } z \geqslant Z_q, \end{cases} \tag{C14}$$

and

$$\frac{\partial \ln T_{\rm mid}}{\partial \ln R} = \frac{R}{T_{\rm mid}}\frac{\partial T_{\rm mid}}{\partial R} = -q_{\rm mid}. \tag{C15}$$

Appendix D
Velocity Extraction Dependency on Planet Position

In this section of the appendix, we want to assess biases in the principal component decomposition of our line-of-sight velocity components; in particular, in the case of a massive embedded planet, how azimuthal velocities can be mislead for radial velocities and vice versa. To this end, we use a 3D hydrodynamical model with the identical setup to the one presented in R. Teague et al. (2019) with one embedded 2 Jupiter mass planet located at 240 au.

We now want to assess how the excited density waves of the planet can introduce velocity perturbations in υ_ϕ and υ_r that break our assumption of the rotational velocity being azimuthally symmetric around the disk's minor axis and dominant over the radial and vertical ones in the line of sight (see Equation (3)). First, we extract the three velocity components υ_ϕ, υ_r, and υ_z from the simulation at $z/r = 0.2$ and then project them onto the sky assuming a moderate disk inclination of 30° along our line of sight (see Equation (2)). Second, we apply Equation (6) to extract υ_ϕ from this line-of-sight velocity. We can then compare our extracted υ_ϕ to our true mean input $\upsilon_{\phi,\rm true}$ from the simulation. For clarity, we additionally subtract the underlying Keplerian rotation from both simulated and measured rotational velocities to show the deviations from Keplerian rotation. In the last step, we change the position of the planet on the sky by varying its azimuthal location ($\phi_{\rm pl}$) in the disk in steps of 45° starting counterclockwise from the redshifted major axis of the disk. So, for example, at 90° it is located exactly at the disk minor axis, at 180° at the blueshifted major axis, and for $\phi_{\rm pl} = 45°, 135°$ right in between both.

First, we want to understand if the planet itself introduces asymmetric perturbations in υ_ϕ. Therefore, we neglect the other two velocity components in the line of sight, which means setting $\upsilon_r = 0 = \upsilon_z$ (see Equation (2)). In panel (a) of Figure D1, we now show the extracted υ_ϕ curves compared to the true mean of the simulation. We see that, irrespective of the planet's azimuthal location, we retrieve the $\delta\upsilon_\phi$ almost perfectly. This means the $\delta\upsilon_\phi$ perturbations induced by the planet are inherently symmetric and do not introduce inaccurate υ_ϕ velocity measurements.

Now, we consider all velocity components along the line of sight. Panel (b) shows the variations in the extraction of $\delta\upsilon_\phi$ introduced by wrongly attributing υ_r (less υ_z) as υ_ϕ, and vice versa. This shows the shortcoming of our velocity extraction method, purely from projection effects along the line of sight. Panel (c) is the subtraction of the extracted $\delta\upsilon_\phi$ curves from the true mean in panel (b). The strongest mismatch occurs for the planet being located right in between disk minor and major axis ($\phi_{\rm pl} = 45°$ and $\phi_{\rm pl} = 135°$). These are the azimuths where υ_ϕ and υ_r equally contribute to the line-of-sight velocity (compare Equation (3)). At these locations it is increasingly difficult to disentangle the velocity components and measure an accurate υ_ϕ. Yet, these are also the azimuthal locations where it is easiest to detect planetary signatures in 2D residual maps, as has been extensively studied in A. F. Izquierdo et al. (2021).

We conclude that even though the amplitude of $\delta\upsilon_\phi$ changes considerably for the planet at different azimuths, the overall shape of the $\delta\upsilon_\phi$ profile in panel (b) is nearly unaffected by this azimuthal dependency. Therefore, we conclude that retrieving the radial locations of pressure gaps through a radially increasing $\delta\upsilon_\phi$ profile is still robustly retrieved. We further note that radiative transfer effects, which we do not consider here for simplicity, can further complicate an accurate measurement of υ_ϕ.

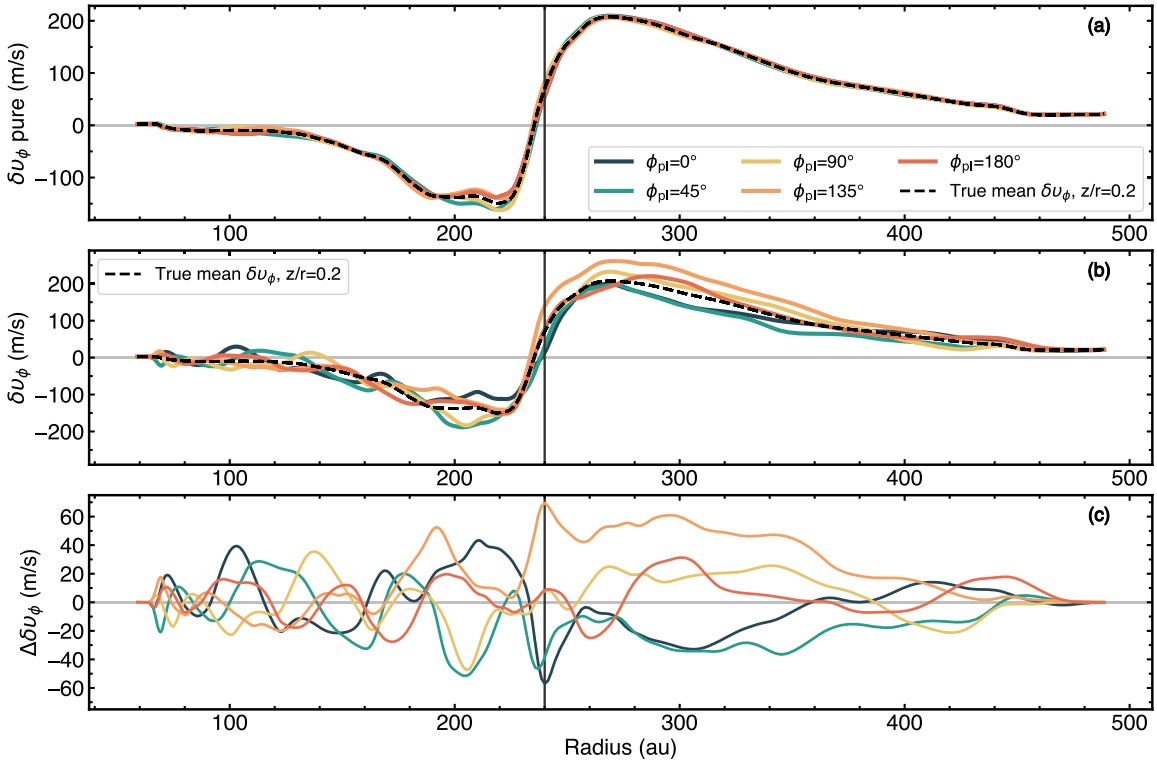

Figure D1. Radial profiles of deviations from Keplerian rotation extracted from a 3D hydrodynamical simulation (R. Teague et al. 2019). The dashed black true mean $\delta\upsilon_\phi$ line is taken directly from the hydrodynamical simulation. The colored $\delta\upsilon_\phi$ lines are extracted from the hydrodynamical data, projected onto the sky, with the `discminer` approach then applied (see Equation (6). The different lines correspond to a planet at different azimuthal locations (ϕ_{pl}) in the disk measured counterclockwise from the redshifted disk major axis.

Appendix E
Complementary Figures

In this subsection, we present complementary figures to the main text. Figure E1 motivates the use of the three different sets of image cubes employed in this Letter, when studying different regions of interest in the disk. Figure E2 shows the rotation curves for all sources and molecular lines targeted by our programm, including the CS J=7-6 transition. Figures E3 and E4 present the $\delta\upsilon_\phi$ radial profiles for ^{13}CO $J = 3$–2 in the disk region beyond and colocated with the continuum emission, respectively. Figures E5 and E6 show the ^{12}CO and ^{13}CO $\delta\upsilon_\phi$ radial profiles for disks, where the pressure variations align with the continuum substructures, in units of kilometeres per second and annotated pressure subtructures as listed in Table 1. The logarithmic midplane pressure derivatives for all disks with available 2D temperature are presented in Figures E7 and E8 focused on the inner and outer disk, respectively. Figure E9 shows the radial profiles of the line-width residuals from the disminer models of the high-resolution image cubes. The CO peak intensity radial profiles of the high-resolution image cubes are plotted in Figure E10. The last Figure E11, shows the ^{12}CO and ^{13}CO $\delta\upsilon_\phi$ radial profiles of the high-surface-brightness sensitivity images in units of kilometers per second focused on the region beyond the dust continuum.

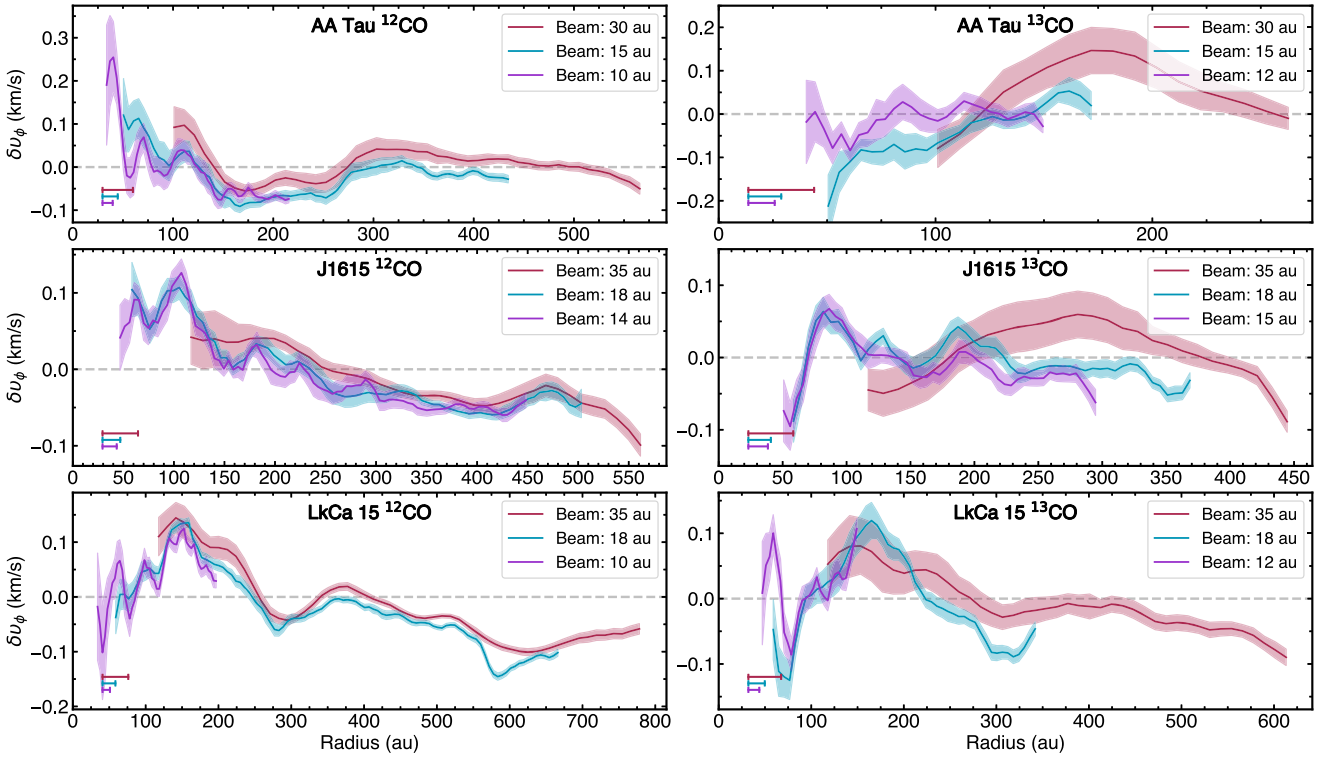

Figure E1. Smoothed radial profiles for δv_ϕ (v_ϕ-v_k) for three different sources using the three sets of continuum-subtracted image cubes at various angular and spectral resolutions These cubes are namely the high-resolution images (red, beam size $< 0\farcs15$), the fiducial images (turquoise, beam size $= 0\farcs15$), and the high-surface-brightness sensitivity images (red, beam size $= 0\farcs30$); see R. Teague et al. (2025) for details. The colored shaded area of the lines shows the standard deviation within each extracted radial annulus. The beam sizes for each image cube are plotted in their respective color in the lower-left corner. The plot shows that the choice of imaging parameters does not negatively affect the analysis products over the scales of interest. In our cases, these are either the innermost disk regions colocated with the continuum or the global scales tracing the outermost disk radii. The δv_ϕ profiles agree within their uncertainties. However, caution is necessary to ensure sufficient angular resolution for rotation curve analysis; otherwise, a beam that is not sufficiently small may smear out the substructures of interest, as can be seen in the overlapping profiles.

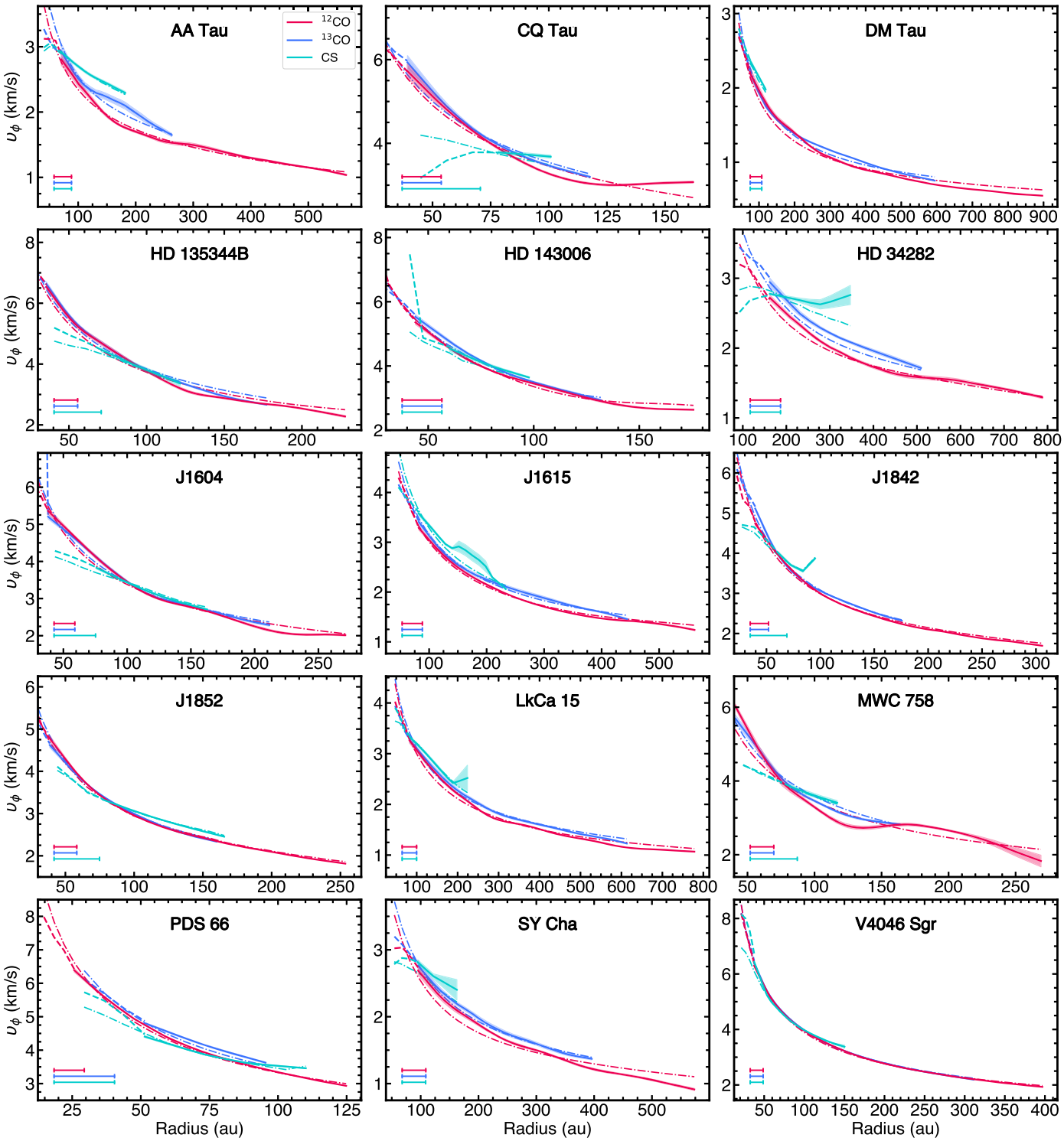

Figure E2. Rotation curves for all sources including the ones for CS $J = 7$–6. For most sources, the CS rotation curves rotate faster than their CO counterparts, further providing evidence for vertical stratification since the CS molecular line emitting height is located closer to the colder midplane and thus shows faster rotation than the CO molecules located at the upper warm irradiated surface layers. The innermost two beam sizes from the center are plotted with dashed lines due to uncertainties in the velocity extraction. The colored shaded area of the lines shows the standard deviation within each extracted radial annulus. The reference Keplerian rotation is plotted as a thin dashed–dotted line for each molecule. The beam sizes for each molecular line are plotted in their respective color in the lower-left corner.

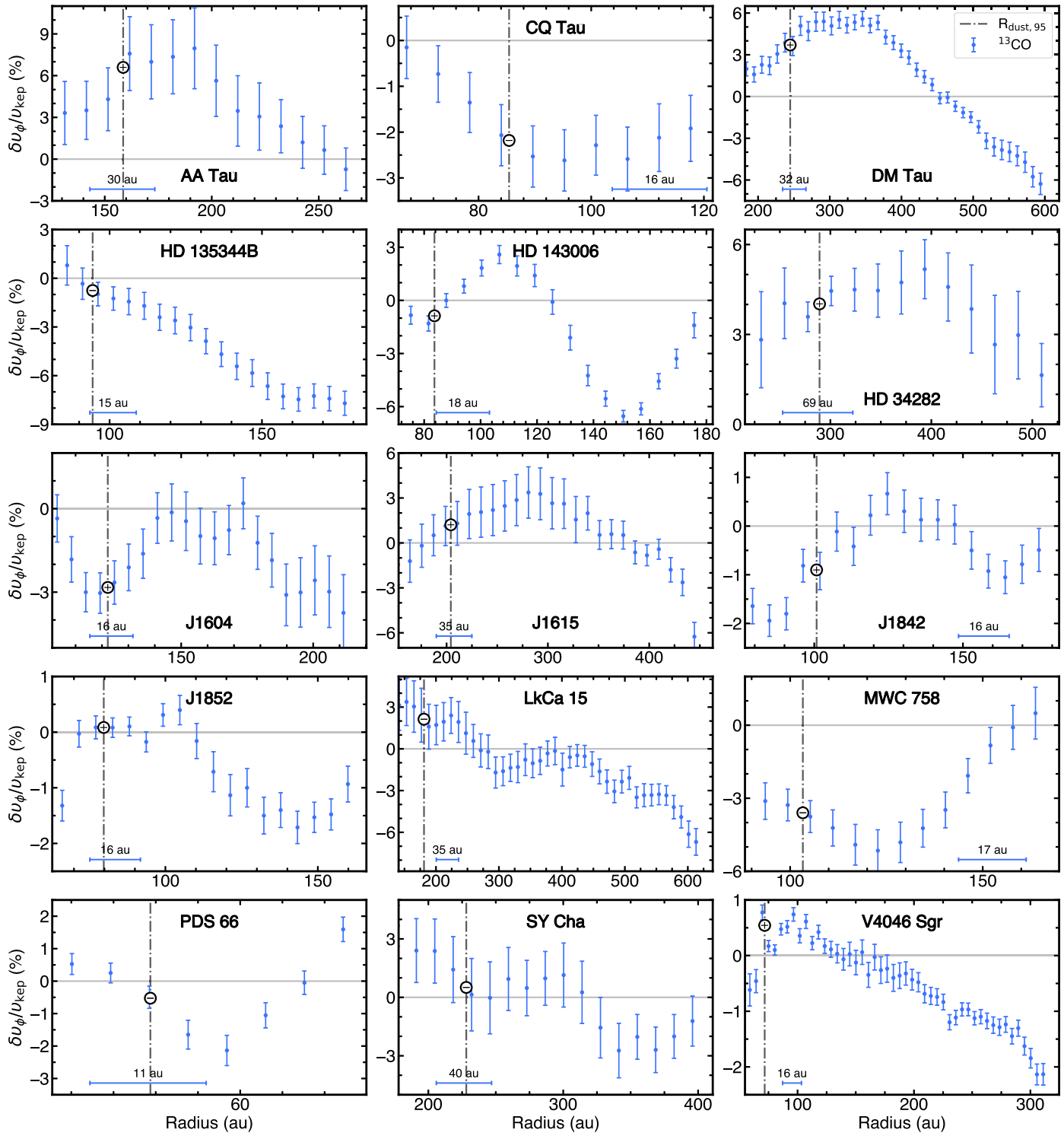

Figure E3. Radial profiles of δv_ϕ for ^{13}CO $J = 3$–2 of all sources focused on the region beyond the continuum substructures using the high-surface-brightness sensitivity images. The error bars show the standard deviation within each extracted radial annulus. The vertical dashed–dotted line indicates the radius that encompasses 95% of the continuum emission, with the signs of the radial derivatives of δv_ϕ marked at this location. The beam size is shown in the lower-left corner.

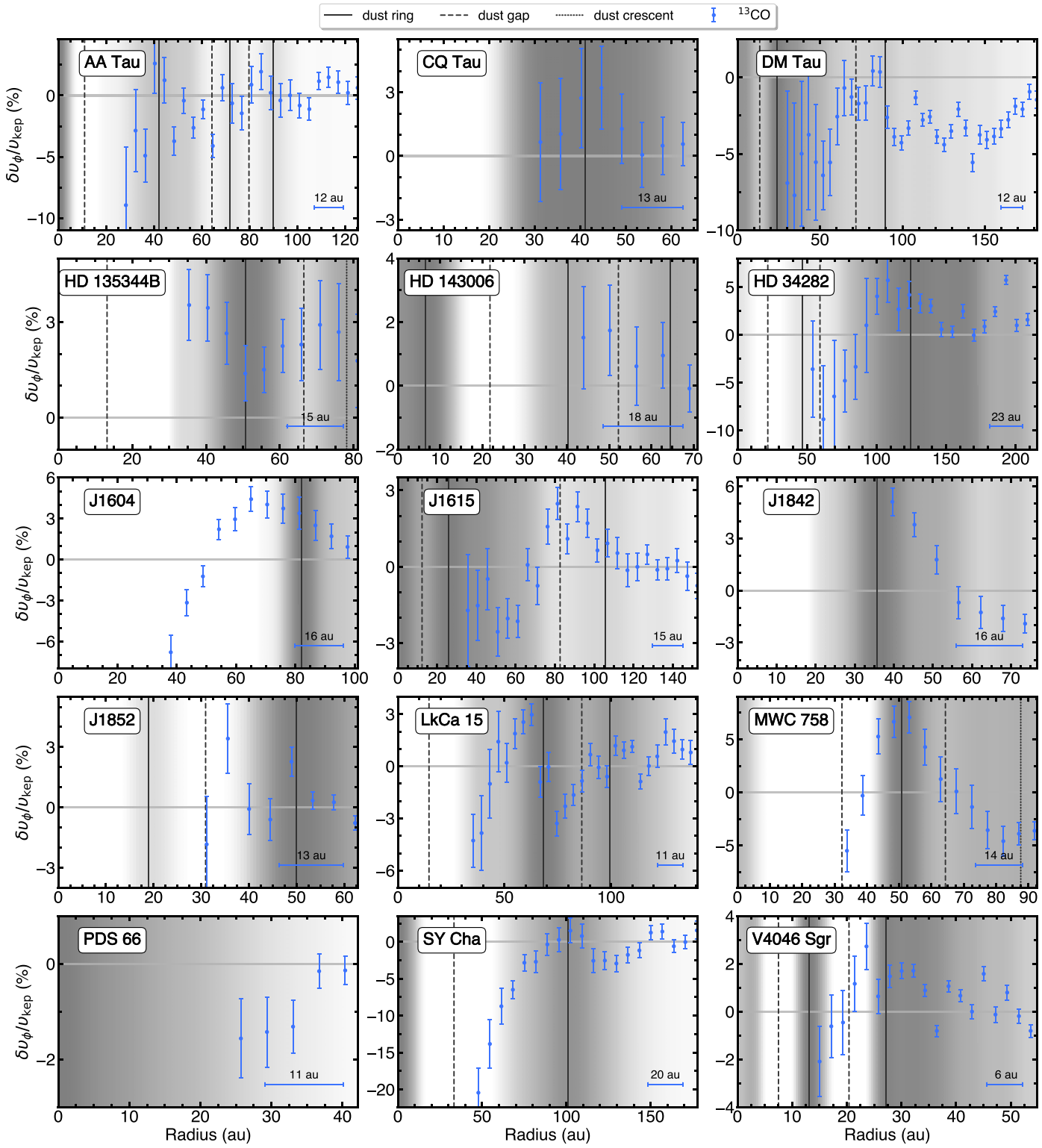

Figure E4. Radial profiles of δv_ϕ for ^{13}CO $J = 3$–2 of all sources focused on the region of the continuum substructures, using the high-resolution images. The profiles are plotted starting at two beam sizes from the disk center, and the error bars show the standard deviation of each bin. The gray background gradient highlights the `frank` radial profiles of the dust continuum emission normalized to its peak. The locations of dust rings, gaps, and crescents are plotted in solid, dashed, and dotted vertical gray lines, respectively (P. Curone et al. 2025). If caused by pressure maxima and minima, then we expect dust rings and gaps to be colocated with a decreasing and increasing δv_ϕ profile, respectively. The beam size is plotted in the lower-right corner.

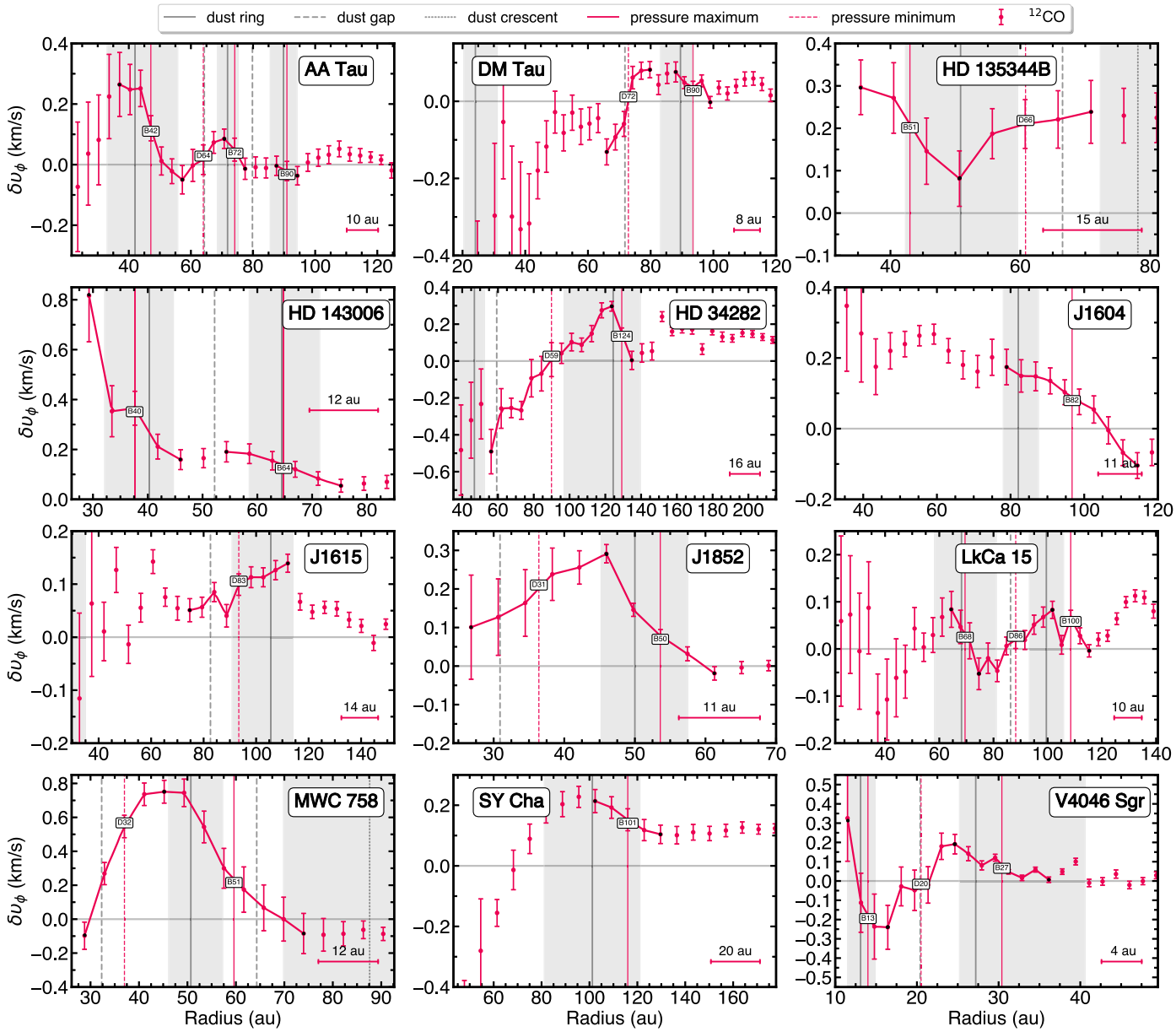

Figure E5. ^{12}CO radial profiles of δv_ϕ for sources with pressure substructures colocated with the continuum substructures using the high-resolution images. δv_ϕ substructures are labeled in each subplot as listed in Table 1. The start and end points of the substructures are annotated with black dots with connecting lines in between them. The vertical dashed and solid red lines indicate the centers of the pressure minima and maxima, respectively. The vertical gray shaded areas show the width of the continuum rings (P. Curone et al. 2025). Additional plot annotations are the same as in Figure E4.

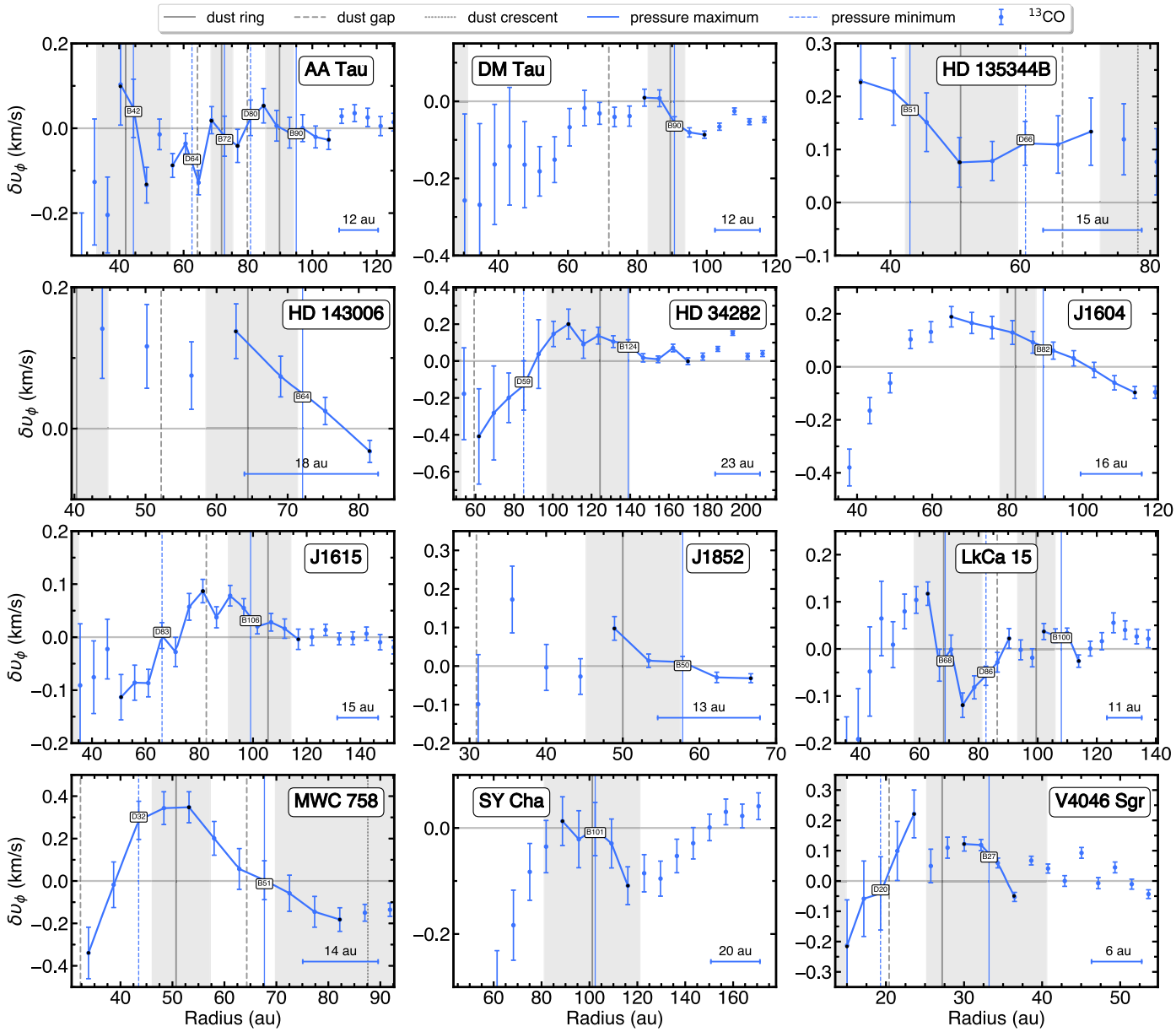

Figure E6. ^{13}CO radial profiles of δv_ϕ for sources with pressure substructures colocated with the continuum substructures using the high-resolution images. δv_ϕ substructures are labeled in each subplot as listed in Table 1. The start and end points of the substructures are annotated with black points with connecting lines in between them. The vertical dashed and solid blue lines indicate the centers of the pressure minima and maxima, respectively. The vertical gray shaded areas show the width of the continuum rings (P. Curone et al. 2025). Additional plot annotations are the same as in Figure E4.

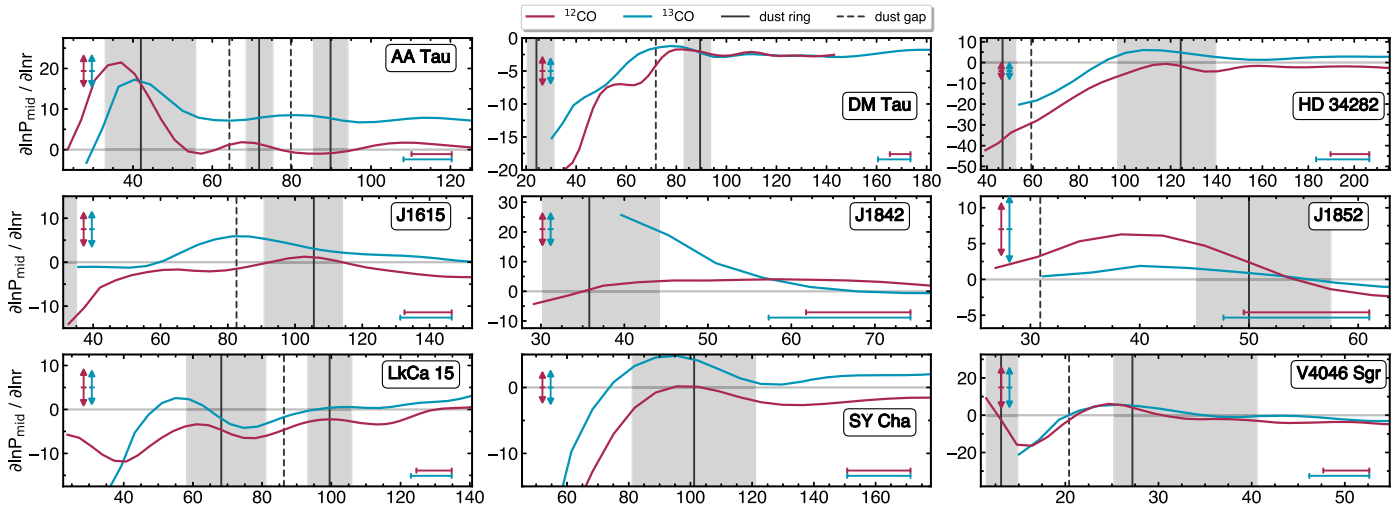

Figure E7. Radial profiles of the logarithmic midplane pressure derivative for all sources with temperature profiles focused on the region of the continuum emission using the high-resolution images. The vertical colored arrows in the upper left show variations in the stellar mass of ±3%, which would result in a shift of the whole profiles up and down. We expect dust rings and gaps to be colocated with $\partial \ln P_{\rm mid}/\partial \ln R = 0$ if induced by pressure maxima and minima (see Figure 1(b)). The vertical gray shaded areas show the width of the continuum rings (P. Curone et al. 2025). The beam sizes for each molecule are plotted in the lower-right corner in their respective color.

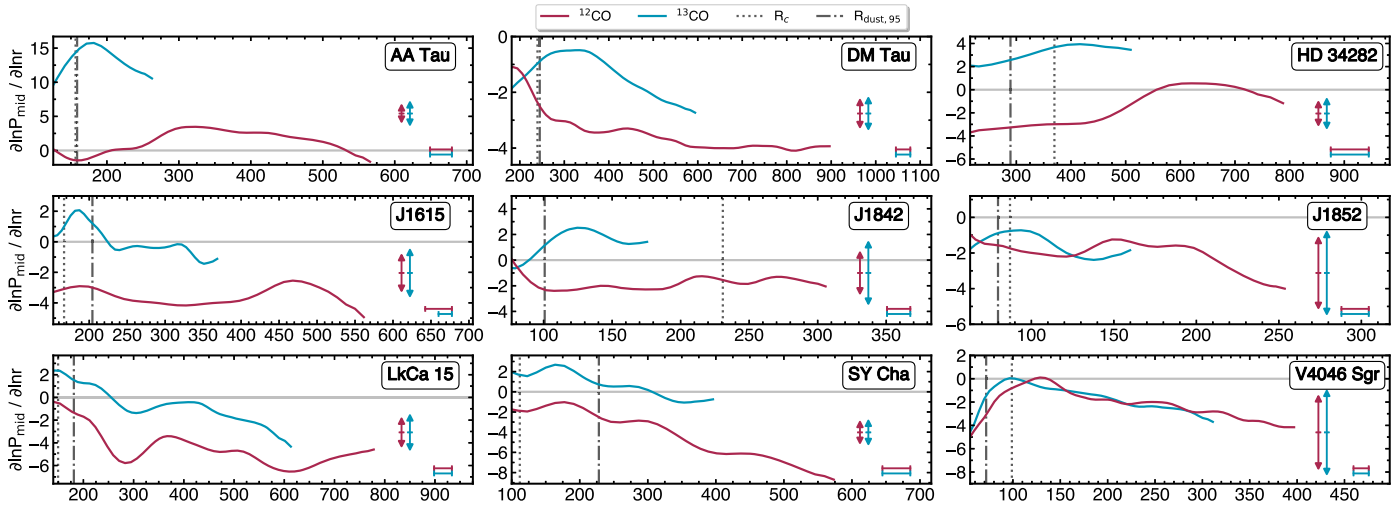

Figure E8. Same as Figure E7 but focused on the disk region beyond the continuum emission using the high-surface-brightness sensitivity images. The dashed–dotted vertical line shows the radius enclosing 95% of the continuum emission (P. Curone et al. 2025) and the dotted vertical line indicates the scale radius R_c for a D. Lynden-Bell & J. E. Pringle (1974) Σ profile derived by C. Longarini et al. (2025).

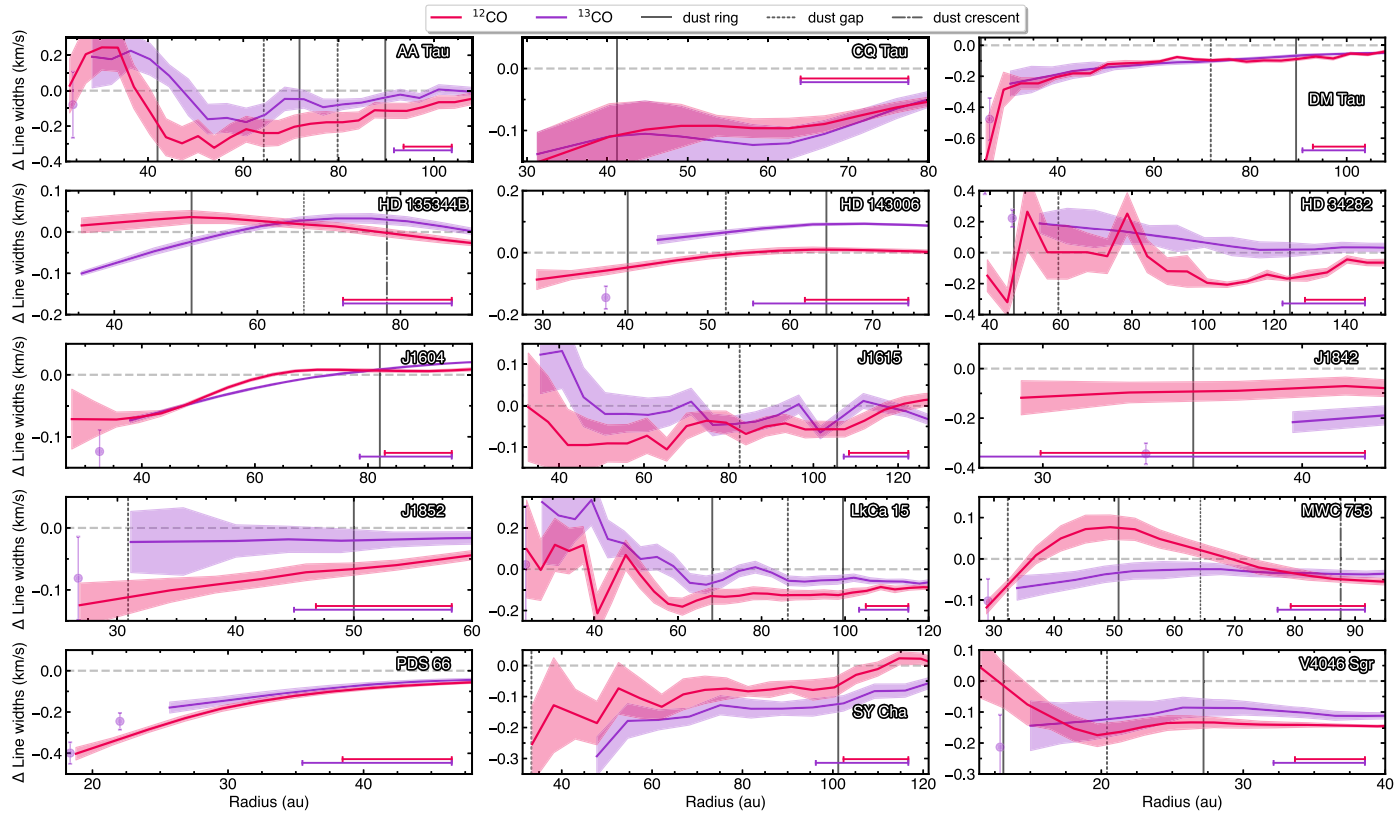

Figure E9. Radial profiles of the CO line-width residuals for the whole sample focused on the region of the continuum emission using the high-resolution images.

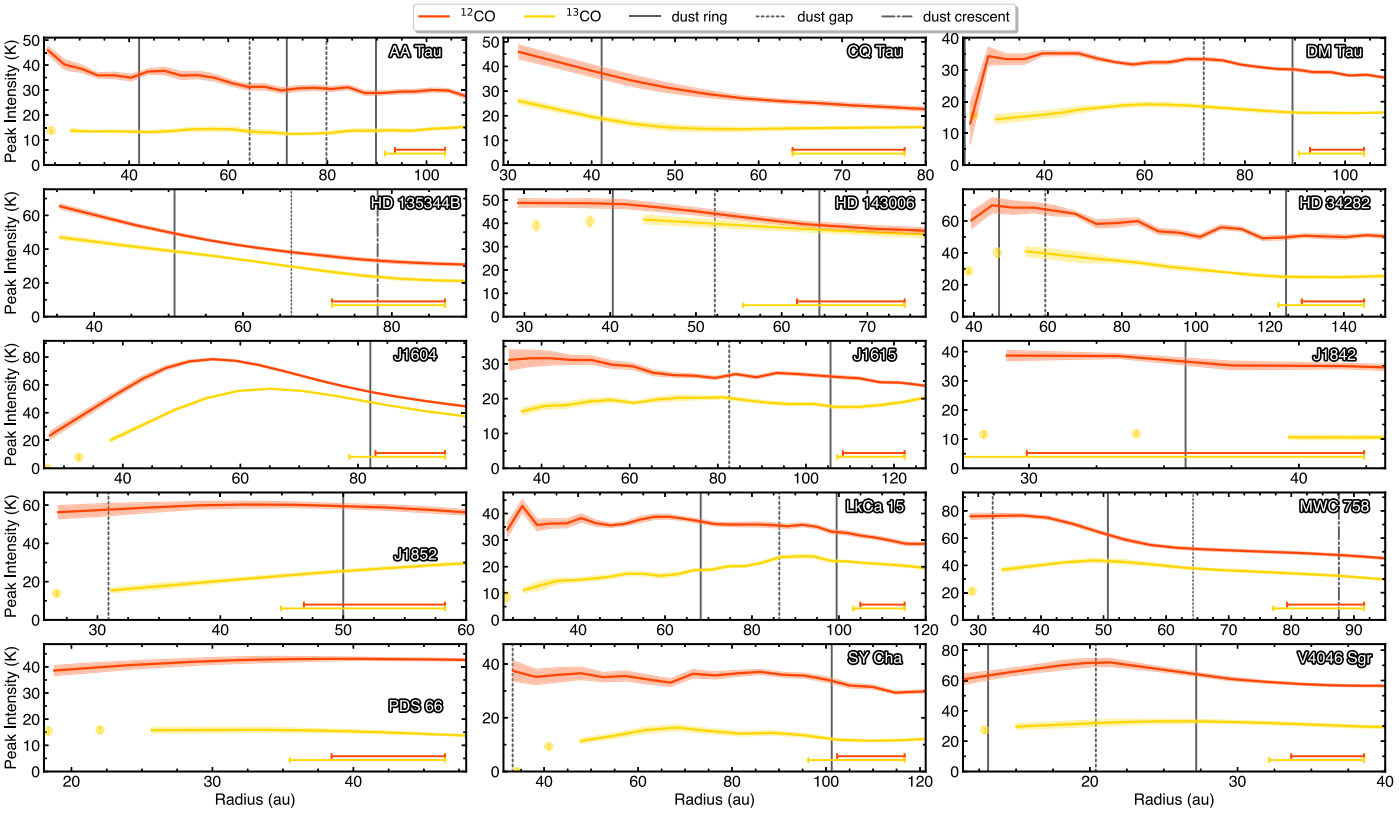

Figure E10. Radial profiles of the CO peak intensities for the whole sample focused on the region of the continuum emission using the high-resolution images.

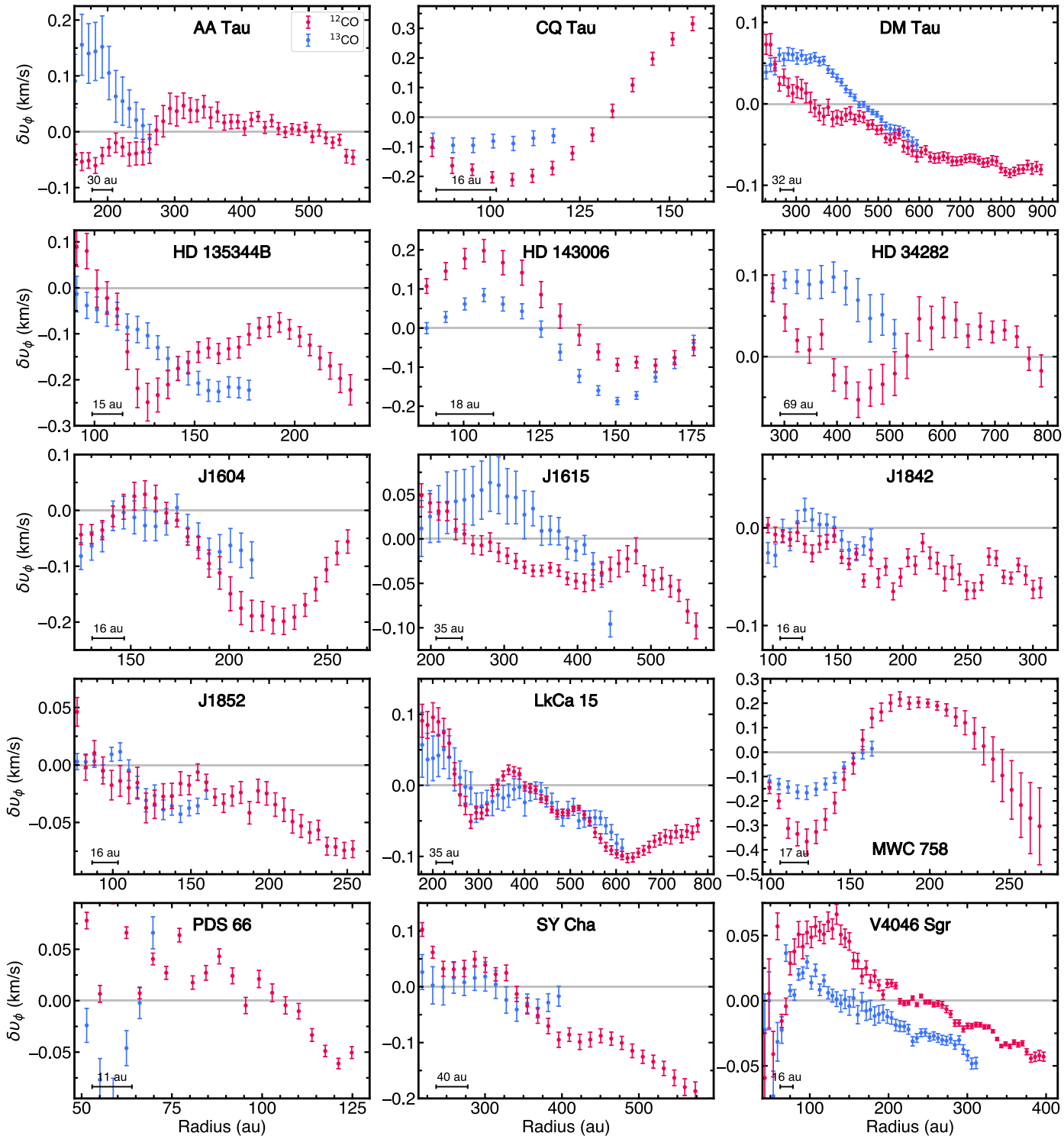

Figure E11. ^{12}CO and ^{13}CO radial profiles of δv_ϕ using the high-surface-brightness sensitivity images. Same as Figures 4 and E3, but here showing δv_ϕ in units of kilometers per second.

ORCID iDs

Jochen Stadler https://orcid.org/0000-0002-0491-143X
Myriam Benisty https://orcid.org/0000-0002-7695-7605
Andrew J. Winter https://orcid.org/0000-0002-7501-9801
Andrés F. Izquierdo https://orcid.org/0000-0001-8446-3026
Cristiano Longarini https://orcid.org/0000-0003-4663-0318
Maria Galloway-Sprietsma https://orcid.org/0000-0002-5503-5476
Pietro Curone https://orcid.org/0000-0003-2045-2154
Sean M. Andrews https://orcid.org/0000-0003-2253-2270
Jaehan Bae https://orcid.org/0000-0001-7258-770X
Stefano Facchini https://orcid.org/0000-0003-4689-2684
Giovanni Rosotti https://orcid.org/0000-0003-4853-5736
Richard Teague https://orcid.org/0000-0003-1534-5186
Marcelo Barraza-Alfaro https://orcid.org/0000-0001-6378-7873

Gianni Cataldi https://orcid.org/0000-0002-2700-9676
Nicolás Cuello https://orcid.org/0000-0003-3713-8073
Ian Czekala https://orcid.org/0000-0002-1483-8811
Daniele Fasano https://orcid.org/0000-0003-4679-4072
Mario Flock https://orcid.org/0000-0002-9298-3029
Misato Fukagawa https://orcid.org/0000-0003-1117-9213
Himanshi Garg https://orcid.org/0000-0002-5910-4598
Cassandra Hall https://orcid.org/0000-0002-8138-0425
Iain Hammond https://orcid.org/0000-0003-1502-4315
Thomas Hilder https://orcid.org/0000-0001-7641-5235
Jane Huang https://orcid.org/0000-0001-6947-6072
John D. Ilee https://orcid.org/0000-0003-1008-1142
Kazuhiro Kanagawa https://orcid.org/0000-0001-7235-2417
Geoffroy Lesur https://orcid.org/0000-0002-8896-9435
Giuseppe Lodato https://orcid.org/0000-0002-2357-7692
Ryan A. Loomis https://orcid.org/0000-0002-8932-1219
Francois Menard https://orcid.org/0000-0002-1637-7393
Ryuta Orihara https://orcid.org/0000-0003-4039-8933
Christophe Pinte https://orcid.org/0000-0001-5907-5179
Daniel J. Price https://orcid.org/0000-0002-4716-4235
Hsi-Wei Yen https://orcid.org/0000-0003-1412-893X
Gaylor Wafflard-Fernandez https://orcid.org/0000-0002-3468-9577
David J. Wilner https://orcid.org/0000-0003-1526-7587
Lisa Wölfer https://orcid.org/0000-0002-7212-2416
Tomohiro C. Yoshida https://orcid.org/0000-0001-8002-8473
Brianna Zawadzki https://orcid.org/0000-0001-9319-1296

References

Andrews, S. M., Teague, R., Wirth, C. P., Huang, J., & Zhu, Z. 2024, ApJ, 970, 153
Astropy Collaboration, Price-Whelan, A. M., Lim, P. L., et al. 2022, ApJ, 935, 167
Ayliffe, B. A., Laibe, G., Price, D. J., & Bate, M. R. 2012, MNRAS, 423, 1450
Bae, J., Isella, A., Zhu, Z., et al. 2023, in ASP Conf. Ser. 534, Protostars and Planets VII, ed. S. Inutsuka et al. (San Francisco, CA: ASP), 423
Barrière-Fouchet, L., Gonzalez, J. F., Murray, J. R., Humble, R. J., & Maddison, S. T. 2005, A&A, 443, 185
Birnstiel, T., Dullemond, C. P., & Brauer, F. 2010, A&A, 513, A79
Boehler, Y., Ménard, F., Robert, C. M. T., et al. 2021, A&A, 650, A59
Bohn, A. J., Benisty, M., Perraut, K., et al. 2022, A&A, 658, A183
Bollati, F., Lodato, G., Price, D. J., & Pinte, C. 2021, MNRAS, 504, 5444
Calcino, J., Norfolk, B. J., Price, D. J., et al. 2024, MNRAS, 534, 2904
CASA Team, Bean, B., Bhatnagar, S., et al. 2022, PASP, 134, 114501
Chang, E., Youdin, A. N., & Krapp, L. 2023, ApJL, 946, L1
Comrie, A., Wang, K.-S., Hsu, S.-C., et al. 2021, CARTA: The Cube Analysis and Rendering Tool for Astronomy, v2.0.0, Zenodo, doi:10.5281/zenodo.3377984
Cui, C., & Bai, X.-N. 2021, MNRAS, 507, 1106
Curone, P., Facchini, S., Andrews, S. M., et al. 2025, ApJL, 984, L9
D'Alessio, P., Calvet, N., & Hartmann, L. 2001, ApJ, 553, 321
Dartois, E., Dutrey, A., & Guilloteau, S. 2003, A&A, 399, 773
Dipierro, G., Price, D., Laibe, G., et al. 2015, MNRAS, 453, L73
Dullemond, C. P., Birnstiel, T., Huang, J., et al. 2018, ApJL, 869, L46
Dullemond, C. P., & Dominik, C. 2004, A&A, 421, 1075
Dullemond, C. P., Isella, A., Andrews, S. M., Skobleva, I., & Dzyurkevich, N. 2020, A&A, 633, A137
Dullemond, C. P., & Penzlin, A. B. T. 2018, A&A, 609, A50
Fasano, D., Winter, A. J., Benisty, M., et al. 2024, A&A, 687, A223
Flock, M., Ruge, J. P., Dzyurkevich, N., et al. 2015, A&A, 574, A68
Galloway-Sprietsma, M., Bae, J., Izquierdo, A. F., et al. 2025, ApJL, 984, L10
Goldreich, P., & Tremaine, S. 1979, ApJ, 233, 857
Goldreich, P., & Tremaine, S. 1980, ApJ, 241, 425
Goodman, J., & Rafikov, R. R. 2001, ApJ, 552, 793
Guzmán-Díaz, J., Mendigutìa, I., Montesinos, B., et al. 2021, A&A, 650, A182
Hacar, A., Alves, J., Burkert, A., & Goldsmith, P. 2016, A&A, 591, A104
Hilder, T., Casey, A. R., Price, D. J., et al. 2025, ApJL, 984, L13
Hsu, C.-Y., Li, Z.-Y., Tu, Y., Hu, X., & Lin, M.-K. 2024, MNRAS, 533, 2980
Hunter, J. D. 2007, CSE, 9, 90
Hyodo, R., Ida, S., & Charnoz, S. 2019, A&A, 629, A90
Izquierdo, A. F., Facchini, S., Rosotti, G. P., van Dishoeck, E. F., & Testi, L. 2022, ApJ, 928, 2
Izquierdo, A. F., Stadler, J., Galloway-Sprietsma, M., et al. 2025, ApJL, 984, L8
Izquierdo, A. F., Testi, L., Facchini, S., Rosotti, G. P., & van Dishoeck, E. F. 2021, A&A, 650, A179
Izquierdo, A. F., Testi, L., Facchini, S., et al. 2023, A&A, 674, A113
Jiang, H., & Ormel, C. W. 2021, MNRAS, 505, 1162
Jiang, H., & Ormel, C. W. 2023, MNRAS, 518, 3877
Kanagawa, K. D., Tanaka, H., Muto, T., Tanigawa, T., & Takeuchi, T. 2015, MNRAS, 448, 994
Keppler, M., Teague, R., Bae, J., et al. 2019, A&A, 625, A118
Kratter, K., & Lodato, G. 2016, ARA&A, 54, 271
Law, C. J., Teague, R., Loomis, R. A., et al. 2021, ApJS, 257, 4
Law, C. J., Teague, R., Öberg, K. I., et al. 2023, ApJ, 948, 60
Lesur, G., Flock, M., Ercolano, B., et al. 2023, in ASP Conf. Ser. 534, Protostars and Planets VII, ed. S. Inutsuka et al. (San Francisco, CA: ASP), 465
Lodato, G. 2007, NCimR, 30, 293
Lodato, G., Rampinelli, L., Viscardi, E., et al. 2023, MNRAS, 518, 4481
Longarini, C., Lodato, G., Rosotti, G., et al. 2025, ApJL, 984, L17
Loomis, R. A., Facchini, S., Benisty, M., et al. 2025, ApJL, 984, L7
Lynden-Bell, D., & Pringle, J. E. 1974, MNRAS, 168, 603
Mannings, V., & Sargent, A. I. 2000, ApJ, 529, 391
Martire, P., Longarini, C., Lodato, G., et al. 2024, A&A, 686, A9
Meheut, H., Casse, F., Varniere, P., & Tagger, M. 2010, A&A, 516, A31
Öberg, K. I., Guzmán, V. V., Walsh, C., et al. 2021, ApJS, 257, 1
Ohashi, S., Kobayashi, H., Nakatani, R., et al. 2021, ApJ, 907, 80
Paardekooper, S. J., & Mellema, G. 2004, A&A, 425, L9
Paneque-Carreño, T., Miotello, A., van Dishoeck, E. F., et al. 2023, A&A, 669, A126
Pezzotta, V., Facchini, S., Longarini, C., Lodato, G., & Martire, P. 2025, A&A, 694, A108
Pinilla, P., Benisty, M., & Birnstiel, T. 2012, A&A, 545, A81
Pinilla, P., Pascucci, I., & Marino, S. 2020, A&A, 635, A105
Pinte, C., Teague, R., Flaherty, K., et al. 2023, in ASP Conf. Ser. 534, Protostars and Planets VII, ed. S. Inutsuka et al., 645
Pinte, C., Ménard, F., Duchêne, G., et al. 2018, A&A, 609, A47
Rab, C., Kamp, I., Dominik, C., et al. 2020, A&A, 642, A165
Rafikov, R. R. 2002, ApJ, 569, 997
Riols, A., & Lesur, G. 2019, A&A, 625, A108
Rosenfeld, K. A., Andrews, S. M., Hughes, A. M., Wilner, D. J., & Qi, C. 2013, ApJ, 774, 16
Rosenfeld, K. A., Chiang, E., & Andrews, S. M. 2014, ApJ, 782, 62
Rosotti, G. P., Teague, R., Dullemond, C., Booth, R. A., & Clarke, C. J. 2020, MNRAS, 495, 173
Saito, E., & Sirono, S.-i. 2011, ApJ, 728, 20
Stadler, J., Benisty, M., Izquierdo, A., et al. 2023, A&A, 670, L1
Stadler, J., Gárate, M., Pinilla, P., et al. 2022, A&A, 668, A104
Takeuchi, T., & Lin, D. N. C. 2002, ApJ, 581, 1344
Teague, R. 2019, JOSS, 4, 1220
Teague, R., Bae, J., Bergin, E. A., Birnstiel, T., & Foreman-Mackey, D. 2018a, ApJL, 860, L12
Teague, R., Bae, J., Birnstiel, T., & Bergin, E. A. 2018b, ApJ, 868, 113
Teague, R., Bae, J., Huang, J., & Bergin, E. A. 2019, ApJL, 884, L56
Teague, R., Benisty, M., Facchini, S., et al. 2025, ApJL, 984, L6
Testi, L., Natta, A., Manara, C. F., et al. 2022, A&A, 663, A98
Uribe, A. L., Klahr, H., Flock, M., & Henning, T. 2011, ApJ, 736, 85
van der Walt, S., Colbert, S. C., & Varoquaux, G. 2011, CSE, 13, 22
Veronesi, B., Longarini, C., Lodato, G., et al. 2024, A&A, 688, A136
Veronesi, B., Paneque-Carreño, T., Lodato, G., et al. 2021, ApJL, 914, L27
Villenave, M., Ménard, F., Dent, W. R. F., et al. 2020, A&A, 642, A164
Virtanen, P., Gommers, R., Burovski, E., et al. 2020, scipy/scipy: SciPy v1.5.3, Zenodo, doi:10.5281/zenodo.4100507
Weidenschilling, S. J. 1977, MNRAS, 180, 57
Whipple, F. L. 1972, in From Plasma to Planet, ed. A. Elvius (New York: Wiley), 211
Wölfer, L., Barraza-Alfaro, M., Teague, R., et al. 2025, ApJL, 984, L22
Yun, H.-G., Kim, W.-T., Bae, J., & Han, C. 2019, ApJ, 884, 142
Zhang, K., Blake, G. A., & Bergin, E. A. 2015, ApJL, 806, L7
Zormpas, A., Birnstiel, T., Rosotti, G. P., & Andrews, S. M. 2022, A&A, 661, A66